LBL-18897
c.2

LBL-18897

RECEIVED
LAWRENCE
BERKELEY LABORATORY

MAR 15 1985

LIBRARY AND
DOCUMENTS SECTION

HEAVY ION RUTHERFORD BACKSCATTERING SPECTROMETRY (HIRBS) FOR NEAR SURFACE CHARACTERIZATION OF ELECTRONIC MATERIALS

K.M. Yu
(M.S. Thesis)

December 1984

TWO-WEEK LOAN COPY

This is a Library Circulating Copy which may be borrowed for two weeks. For a personal retention copy, call Tech. Info. Division, Ext. 6782.

Lawrence Berkeley Laboratory
University of California
Berkeley, California 94720

Prepared for the U.S. Department of Energy
under Contract DE-AC03-76SF00098

Center for Advanced Materials

LBL-18897
c.2

DISCLAIMER

This document was prepared as an account of work sponsored by the United States Government. While this document is believed to contain correct information, neither the United States Government nor any agency thereof, nor the Regents of the University of California, nor any of their employees, makes any warranty, express or implied, or assumes any legal responsibility for the accuracy, completeness, or usefulness of any information, apparatus, product, or process disclosed, or represents that its use would not infringe privately owned rights. Reference herein to any specific commercial product, process, or service by its trade name, trademark, manufacturer, or otherwise, does not necessarily constitute or imply its endorsement, recommendation, or favoring by the United States Government or any agency thereof, or the Regents of the University of California. The views and opinions of authors expressed herein do not necessarily state or reflect those of the United States Government or any agency thereof or the Regents of the University of California.

HEAVY ION RUTHERFORD BACKSCATTERING SPECTROMETRY(HIRBS) FOR THE NEAR SURFACE CHARACTERIZATION OF ELECTRONIC MATERIALS

Kin Man Yu

M.S. Thesis

Lawrence Berkeley Laboratory
and
Department of Materials Science and Mineral Engineering
University of California
Berkeley, California 94720

December 1984

ABSTRACT

The use of heavy ion projectiles for Rutherford Backscattering Spectrometry(RBS) provides several potential advantages over conventional RBS with ^{4}He beams. Among these advantages are the improved mass resolution for heavy elements (>50 AMU) and the increased accessible depth of analysis. A series of experiments using 20 MeV ^{16}O beam backscattered from a variety of targets was performed in order to examine the potential advantages of heavy ion RBS in the near surface characterization of semiconductors with masses greater than 50 AMU. Important questions such as mass resolution, depth resolution, isotopic effects, absolute sensitivity and minimum detectable limit of impurities were investigated. Ion implantations and multiple layered structures on GaAs substrates as well as metal germanide systems were studied. The development of the method in conjunction with the channeling technique is also discussed.

Acknowledgements

I am especially grateful to Professor Eugene E. Haller for his guidance and support throughout the course of this work. My sincere thanks to Dr. Joseph M. Jaklevic for his supervision, time and patience and most of all, for offering me the opportunities to new challenges in the past two years.

Special thanks to Professor Nathan Cheung of the Electrical Engineering and Computer Science Department and Professor Eicke Weber of the Materials Science and Mineral Engineering Department for reviewing and making many valuable comments on this thesis.

I also like to acknowledge the technical assistance of several members of the Department of Instrument Science and Engineering at Lawrence Berkeley Laboratory especially W. L. Searles, N. W. Madden and K. S. Luchini. The HIRBS measurements were made possible through the cooperation and assistance of R. Stokstad, R. M. Larimer and the staff of the 88" cyclotron at LBL. The ion-implanted GaAs samples and the multiple layered metallization samples were provided by S. Eglash, J. Miller and J. Amano of Hewlett Packard Research Laboratories. The Au/Pd/Ge samples were provided by P. N. Luke.

This work was supported by the Director's Office of Energy Research, Office of Basic Energy Sciences, Materials Science Division of the U. S. Department of Energy under Contract No. DE-AC03-76SF00098.

TABLE OF CONTENTS

Page

1. INTRODUCTION.....1

1.1 Rutherford Backscattering Spectrometry (RBS) as a Near Surface Characterization Technique for Electronic Materials..1

1.2 Motivation for the Development of Heavy Ion RBS.....4

2. RUTHERFORD BACKSCATTERING SPECTROMETRY(RBS).....7

2.1 Kinematic Factor K.....8

2.2 Scattering Cross Section σ.....11

2.3 Energy Loss dE/dx.....12

2.4 Energy Straggling and System Energy Resolution.....19

2.5 Mass Resolution and Depth Resolution.....22

3. CONVENTIONAL RUTHERFORD BACKSCATTERING SPECTROMETRY (α-RBS)..24

3.1 Introduction.....24

3.2 Examples of Analysis.....26
3.2.1 Thin Films Studies.....26
3.2.2 Ion-Implantation Analysis.....31
3.2.3 Lattice Location of Impurity Atoms and Lattice Disorder.....34

3.3 Limitations.....41

4. HEAVY ION RUTHERFORD BACKSCATTERING SPECTROMETRY(HIRBS).....46

4.1 Introduction.....46

4.2 Important Parameters.....50
4.2.1 Energy Straggling.....50

4.2.2 Energy Resolution, Mass Resolution and Depth Resolution....53

4.3 Instrumentation....56

4.4 Applications (Experimental Results)....61
4.4.1 Mass Resolution Study....62
4.4.2 Ion Implantation Study....64
4.4.3 Germanide Formation Study....70
4.4.4 Multiple Layers Structures on Compound Semiconductors....73

4.5 Future Development--HIRBS/Channeling....76
4.5.1 Dechanneling in a Perfect Crystal....76
4.5.2 Dechanneling by Defects....78

5. SUMMARY....81

5.1 Advantages....81

5.2 Limitations....82

REFERENCES....85

HEAVY ION RUTHERFORD BACKSCATTERING SPECTROMETRY FOR THE NEAR SURFACE CHARACTERIZATION OF ELECTRONIC MATERIALS

1 INTRODUCTION

1.1 Rutherford Backscattering Spectrometry(RBS) As A Near Surface Characterization Technique For Electronic Materials

Rutherford Backscattering Spectrometry(RBS) is a very powerful surface and near surface characterization technique (100 to 1000Å) especially for electronic materials. The strength of RBS as an analytical technique lies in the fact that it can provide depth information without employing any physical or chemical sectioning technique and it can provide quantitative analysis without reference of standards of similar composition. In addition to exhibiting these advantages, RBS is also fast, simple and non-destructive.

The basic experimental arrangement consists of three major components, namely, the beam generation system, the scattering chamber and the data handling system. The measurement consists of directing a collimated monoenergetic beam of charged particles incident on a target, detecting these particles backscattered at a particular angle and measuring the resultant energy spectrum of detected particles. The theoretical basis for the interpretation of the spectrum is well understood from nuclear physics.

In a conventional RBS experiment, the kinds of information one can obtain include (1) identification of elemental

constituents, (ii) depth and the thickness of impurity layers, and (iii) concentration profile. The elemental information is provided through the kinematic scattering factor K which is simply the ratio of the energy of the projectile after and that before the collision. K is derived from equations expressing the conservation of energy and momentum and is different for different pairs of projectile and target atoms. Therefore K can be looked upon as a unique identifier for different elements for a certain kind of projectile ion. The depth information can be obtained through the energy loss (dE/dx) characteristics of the projectile in the target materials. Finally one can get the concentration of certain elements in the target by the total yield, i.e., the total number of particles backscattered by the desired element intercepted by the detector, the probability of collision (the Rutherford scattering cross section σ), and the total number of particles incidented on the sample.

Figure 1.1 shows a schematic energy spectrum obtained in a RBS experiment. The target is a compound of two elements A and B with A heavier than B. The abscissa represents the channel number corresponding to a particular value on the energy scale and the ordinate gives the yield per channel. By measuring the location of the edges one gets the masses of A and B. The heights of the edges in the spectrum represent the concentrations of the two elements in the compound. A real RBS spectrum is, however, more complicated. One major complication is the energy loss straggling which arises from the statistical fluctuation of the total energy loss, the sum of numerous small energy losses

of the projectiles in the target. Another more important effect is the detector energy resolution. As a result, the energy spectrum is broadened and the step-like edges in the spectrum will be smoothened out.

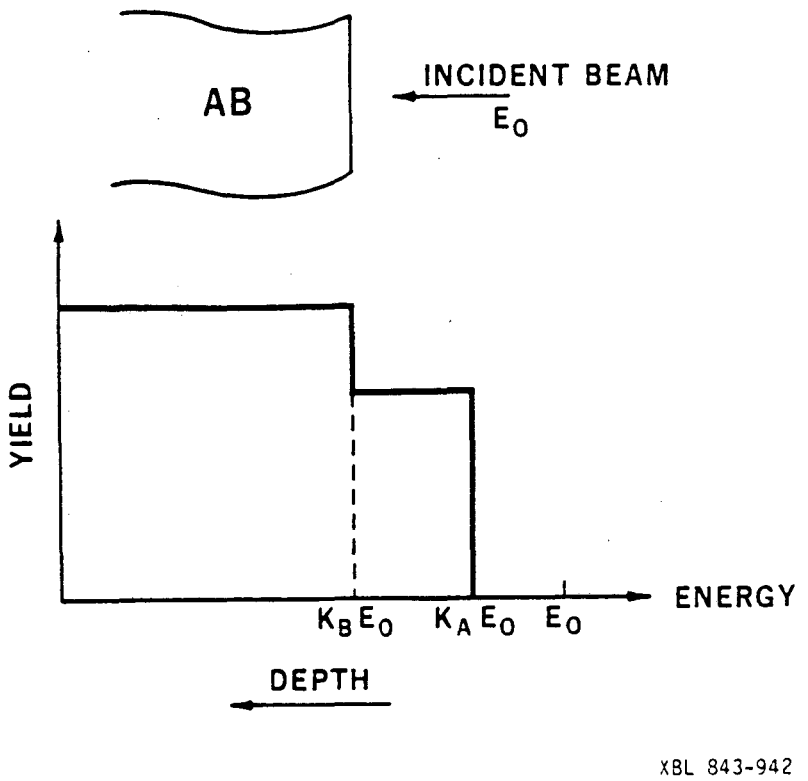

Fig. 1.1 Theoretical spectrum for a RBS experiment on a compound target AB with A heavier than B.

RBS did not become widely applied to real scientific problems until the early 1960s when solid-state detectors with good energy resolution became available. With the rapid growth of the electronic industry and the introduction of planar technology in semiconductor device fabrication, RBS as a near surface characterization technique found more and more applications in electronic

materials research. Since then, a number of problems have been studied with RBS including surface impurities identification [1-3], impurity distribution in depth especially dopant concentration profiles in semiconductors with ion implantation or diffusion process[4-6], metal/semiconductor interfacial reactions [7-11], and metal-metal interaction analyses[12-15]. By directing the particle beam into a major crystallographic axis of the target, a technique called channeling, RBS is also used to analyze crystallinity problems such as depth distribution of lattice disorder caused by radiation damage[16,17], location of impurity atoms in the lattice sites[18-21], and composition and thickness of amorphous surface layers[22].

RBS is, however, not limited to the applications in the field of electronic materials. The method is also applied to nuclear energy technology and materials science where near surface characterization is important. Cladding materials, first wall erosion, corrosion, thin film reactions, oxiations and superconducting and magnetic thin films have also been studied with RBS.

1.2 Motivations for the Development of Heavy Ion RBS

With the increasing sophistication of the devices employed by the electronic industry, many of the existing characterization techniques are becoming inadequate. Recently, the increasing demand for high speed, high density large-scale integrated

circuits led to the design of devices with very shallow junctions and the development of compound semiconductors such as GaAs and InP. As a result, more complicated metallization schemes with multiple layered structure are needed.

For many of the structures, analysis by conventional RBS with ^{4}He ion beam is difficult because of some inherent weaknesses in the method. These include insensitivity to light elements in heavy substrates, poor lateral resolution due to beam size and the lack of chemical information. But the most important limitation when applied to III-V compounds is its poor mass resolution for heavy elements (M>50AMU). This arises from the fact that the difference in the energies of the particles backscattered from targets of adjacent mass becomes more and more indistinguishable as the target becomes heavier. In other words the K factor in RBS is rather insensitive to the change of target mass for heavy targets. This limits its applications considerably, especially in the analysis of multiple layered structures and the investigations of problems in III-V compound semiconductor materials and devices.

The use of ions heavier than ^{4}He as projectiles in RBS results in an improvement of mass resolving power while it preserves the basic advantages of conventional RBS. In fact, we have demonstrated that adjacent elements can be resolved for elements as heavy as Au (M=197AMU). This makes heavy ion RBS (HIRBS) a very promising technique in near surface characterization for compound semiconductors and multiple layered metallization schemes. In addition to the mass resolution improvement

achieved, a decrease in the relative energy loss $(dE/dx)/E_0$ is also attainable by HIRBS (where E_0 is the incident energy of the projectiles). This results in an increase in the accessible depth of analysis for the method.

2. RUTHERFORD BACKSCATTERING SPECTROMETRY(RBS)

Rutherford Backscattering Spectrometry was established following the discoveries of Rutherford and of Geiger and Marsden [23,24]. The original experiment by Geiger and Marsden was to confirm the atomic model proposed by Rutherford. The basic idea of the experiment is to shoot energetic charged particles (4 to 8 MeV alpha particles from a radioactive source) at a group of atoms and to examine the distribution in angle of the particles after passing through the atoms. This experiment was purely of nuclear physics interest and the analytical nature of the scattering method was not fully realized until the late 1950s [25].

The basic physics of RBS is appealing because of its uncomplicated nature. As a matter of fact, there are only three most important physical concepts involved in this technique each of which gives a specific kind of information:

(1) the kinematic scattering factor K which gives elemental information,

(2) the scattering cross-section σ which gives quantitative information of the atomic composition of the target, and

(3) the observed energy loss dE/dx of an projectile ion when penetrating through the target which can be interpreted to give depth information of the target layers without sectioning.

2.1 The Kinematic Factor K

When a beam of monoenergetic charged particles is incident on a solid surface, it can undergo a number of interactions with the atoms in the solid. Some of these particles will be scattered due to interactions with individual atoms at and near the surface. If the incoming energy E_0 of the projectile particles is lower than the energy needed for nuclear reaction between these particles and the target elements, the particles will be elastically scattered and the energy of the scattered particles at a specific scattered angle will be a function only of the particle mass M_1, the target mass M_2, and the angle of scattering. With the above assumptions, the collision process between a projectile particle and a target atom is called an elastic collision. Figure 2.1 shows the geometry of such a collision. The scattered energy $E=KE_0$ where K is known as the kinematic factor which is determined solely by kinematic consideration. Using the principles of conservation of energy and momentum, one can show that [26]

$$K = \left(\frac{(M_2^2 - M_1^2 \sin^2\theta)^{\frac{1}{2}} + M_1\cos\theta}{M_1 + M_2}\right)^2 , \qquad (2.1)$$

where M_1 is the projectile mass, M_2 is the target mass and θ is the scattering angle. For a given kind of projectile particles at a particular scattering angle, K is uniquely defined for any given target element. As a result, different elements can be

identified by measuring the energies of the scattered projectiles.

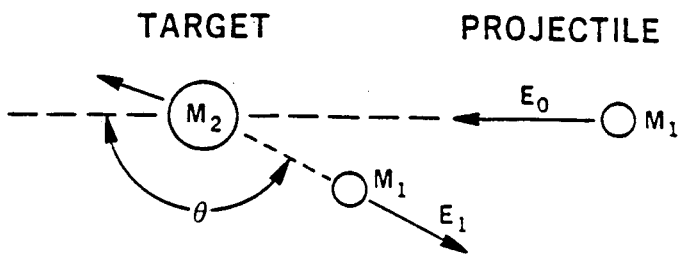

$$K \equiv E_1/E_0$$

$$K(\theta=180°) = \left[\frac{1 - M_1/M_2}{1 + M_1/M_2}\right]^2$$

$$\frac{d\sigma}{d\Omega} \approx \left[\frac{Z_1 Z_2 e^2}{4E_0}\right]^2 \mathrm{SIN}^{-4}\,\theta/2 \qquad M_1 \ll M_2$$

XBL 834-9456

Fig. 2.1 Geometry of an elastic collision process between a projectile atom with mass M_1 and a target atom with mass M_2

Figure 2.2 shows the relationship between K and M_2/M_1 for different scattering angle θ. For scattering angles smaller than 90°, i.e. the forward scattering case, K is relatively insensitive to the change in target masses. Since the K values determine the scattered energies, it is desirable to have the slope of the K versus M_2/M_1 curve as large as possible in order to achieve good mass resolving power. As a result, the backscattering geometry with θ greater than 90° is favorable as far as mass

resolution is concerned. In fact, one tries to make θ as close to 180° as possible. It is also worth noticing that in the backscattering geometry, when M_2/M_1 is smaller than 1, K is 0. In other words, a projectile colliding with a stationary atom with mass equal to or smaller than its own cannot be scattered backward, but only forward.

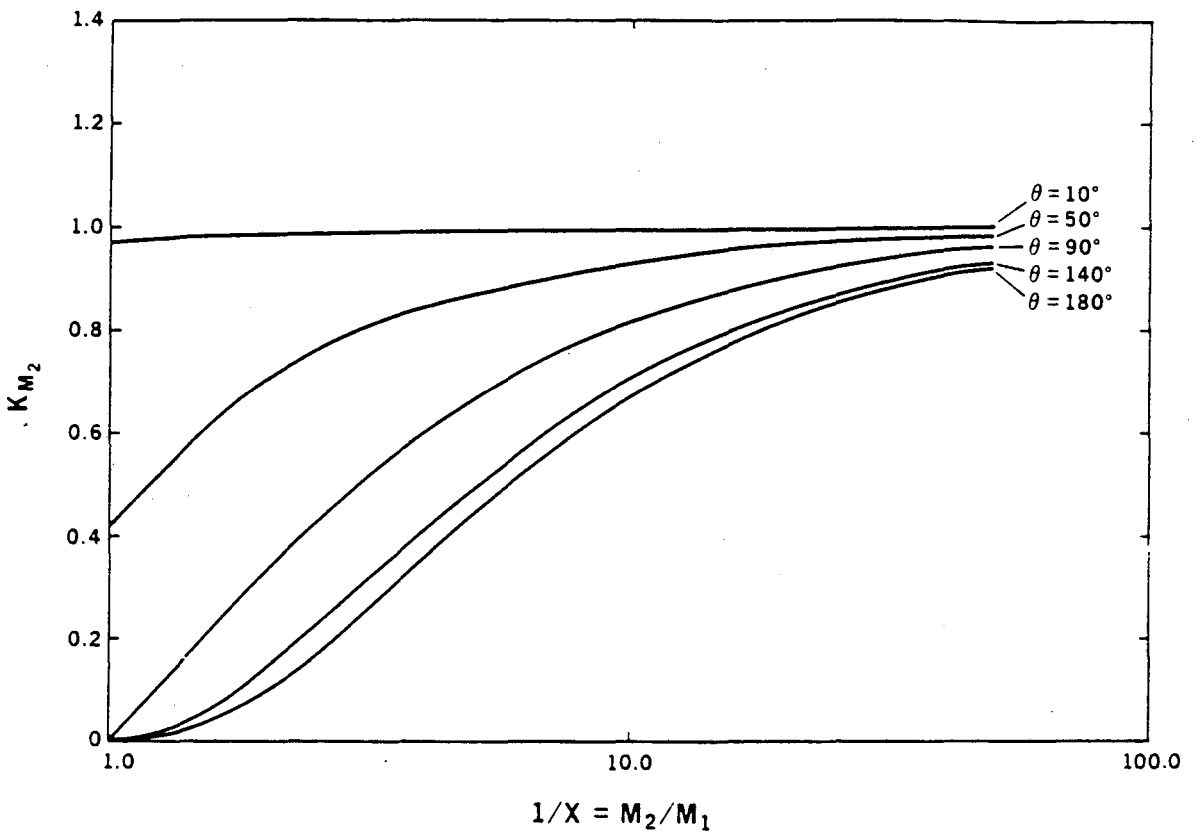

XBL 845-1740

Fig. 2.2 The kinematic factor K plotted as a function of the mass ratio $1/x = M_2/M_1$ for different scattering angle θ.

2.2 Scattering Cross Section σ

The term cross section used in nuclear physics is a measure of the probability of the occurrence of a given process. Rutherford scattering cross section is, therefore, a measure of the probability that a particle will have nuclear scattering with a target atom. The concept of differential scattering cross section is introduced in order to account for the directionality of the scattered particles. The differential scattering cross section can be thought of as a small area within the total cross section σ. When a particle hits within this small area, it is scattered into a solid angle $d\Omega$ centered around the scattering angle θ. It is therefore a measure of the probability that a particle will be scattered through a solid angle whose value lies between Ω and $\Omega+d\Omega$, Ω is the detector solid angle which is typically a few millisteradian. This parameter enables RBS to obtain quantitative information about the target. Generally, the total of detected backscattered particles A can be related to the amount of material in the target by

$$A=d\sigma/d\Omega \; QNt \; d\Omega \qquad (2.2)$$

where Q is the total number of incident particles and Nt is the number of target atoms per unit area. Since A, Q, Ω are measurable quantities, the number of target atoms Nt can be calculated if σ is known. In particular, in the case of thin film analysis, assuming that N is the bulk atomic density of the

material, the thickness of the film can be measured .

The expression for the Rutherford differential scattering cross section was developed through the assumption of Coulombic interaction between target and projectile and is written as

$$\frac{d\sigma}{d\Omega} = \left(\frac{Z_1 Z_2 e^2}{4E}\right)^2 \frac{4}{\sin^4\theta} \frac{((1-((M_1/M_2)\sin\theta)^2)^{1/2}+\cos\theta)^2}{(1-((M_1/M_2)\sin\theta)^2)^{1/2}} \qquad (2.3)$$

where Z_1, Z_2 are the atomic numbers of the projectile and the target nuclei respectively and E is the incident energy. The expression shows that the total of backscattered particles has a $(Z_1 Z_2/E)^2$ dependence. The Z^2 dependence shows why heavy elements in a light matrix are a favorable case for analysis.

2.3 Energy Loss dE/dx

As an energetic ion wanders its way through the target, it slows down and its kinetic energy decreases. This energy loss or the stopping of the projectile ion in matter consists of two processes:

(1) energy loss due to interaction of the ion with the target electrons--electronic or inelastic stopping process, and

(2) energy loss due to interaction of the ion with the target nuclei--nuclear or elastic stopping process.

These two processes are largely independent of each other so that the energy loss can be separated as follows:

$$\frac{dE}{dx} = \frac{dE}{dx}\Big]_{electronic} + \frac{dE}{dx}\Big]_{nuclear} \tag{2.4}$$

For almost a century, a lot of theoretical and experimental effort has been spent on the calculation of the stopping of energetic ions in matter [27]. The nuclear stopping process can simply be treated as the kinetic scattering of two screened particles. This large angle scattering process is highly unlikely and can be treated as a secondary process. The main contribution to the total energy loss of an energetic ion (MeV energy range) in matter stems from its interaction with the target electrons. This interaction is the excitation or ionization of the target atoms to which the ion comes sufficiently close. These changes of state are caused by the Coulomb force, which can give a sharp impulse to an electron as the ion moves swiftly by. The energy transferred to an electron represents a loss of kinetic energy of the moving ion, which therefore will slow down and eventually stop. The ion moves by the atoms with a velocity v, which we assume is so great (MeV ion) that the ion hardly changes its direction in this kind of interaction.

Various theoretical models had been used for the calculation of $dE/dX]_{electronic}$ [28-30]. The Bethe-Bloch formula was developed using quantum mechanical calculations

$$\frac{dE}{dx}\Big]_{electronic} = NZ_2 \left[4\pi(Z_1 e^2 / m_e v_1^2\right] L \tag{2.5}$$

where Z_1 and Z_2 are the atomic numbers of the projectile ion and

the target element respectively, v_1 is the velocity of the projectile ion, m_e is the mass of electron, N is the atomic concentration of the target and L is the stopping number. The stopping number L can be expressed as $L=\ln(2m_e v_1^2/I)$ [28] where I is an empirical parameter representing the average over the various excitations and ionizations of the electrons in the target atom. Since L varies slowly with particle energy, dE/dx therefore varies as $1/v^2$, or inversely with the particle energy.

This can be explained by seeing that because the charged particle spends a longer time in the vicinity of any given electron when its velocity is low, the impulse felt by the electron, and hence the energy transfer is largest. For ions with energies in the MeV range such as used in backscattering spectrometry, the nuclear stopping process can be neglected and $dE/dX]_{total} \approx dE/dX]_{electronic}$.

With the knowledge of energy loss characteristics of projectile ions in the target, a depth scale of the target can be established from the energy of the backscattered particles. The energy of a projectile ion at any depth x below the surface of the target can be written as

$$E(x) = E_0 - \int_0^x (dE/dx)dx \qquad (2.6)$$

Since dE/dx is a function of energy, not x, the above equation cannot be evaluated easily. A simple solution of the problem is to treat x as a function of E and uses the surface

energy approximation where dE/dX is evaluated at the surface energy E_0 [26]. Therefore equation (2.6) becomes

$$x = (E_0 - E)(dE/dx]_{E_0}]^{1} \tag{2.7}$$

In general, the surface energy approximation gives very good results as long as the energy region of interest corresponds to the submicron range in distance.

Since the total energy loss for a projectile ion penetrating a target material with depth Δx ($\Delta E = (dE/dx)\Delta x$) is also dependent on areal density(atoms/cm^2) of the target material, it is convenient to define a density independent parameter ε, the stopping cross section such that

$$\varepsilon = (\frac{1}{N} \bullet \frac{dE}{dx}) \tag{2.8}$$

The conventional unit for ε is eV-cm^2/atom.

The conversion of the energy difference ΔE between the particles scattered at the target surface and those scattered at a depth t below the target surface can be written in the following way:

$$\Delta E = [S_0]\ t \tag{2.9}$$

where [S] is called the energy loss factor. With reference to figure 2.3, the energy loss factor can be expressed as

$$[S] = \frac{K}{\cos\theta_1}\frac{dE}{dx}\Big]_{in} + \frac{1}{\cos\theta_2}\frac{dE}{dx}\Big]_{out} \qquad (2.10)$$

where $dE/dx]_{in}$ is the stopping power along the inward path and $dE/dx]_{out}$ is the stopping power along the outward path of the projectile ion. With the surface energy approximation, equation (2.10) becomes

$$[S_0] = \left(\frac{K}{\cos\theta_1}\frac{dE}{dx}\Big]_{E_0} + \frac{1}{\cos\theta_2}\frac{dE}{dx}\Big]_{KE_0}\right) \qquad (2.11)$$

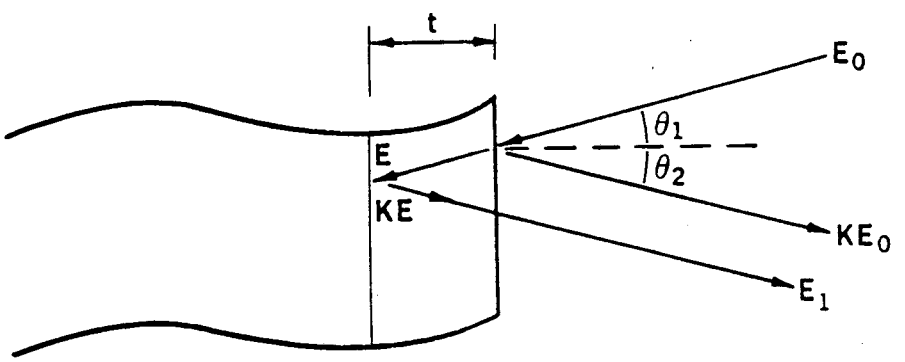

XBL 842-626

Fig. 2.3 Schematic diagram of a RBS experiment showing the incident and the scattering angle θ_1 and θ_2, the back-scattered energy from surface KE_0 and from a depth t.

In terms of the stopping cross section, we can also write

$$\Delta E = [\varepsilon_0]\, Nt \qquad (2.12)$$

where

$$[\varepsilon_0] = \left(\frac{K}{\cos\theta_1}\ \varepsilon(E_0) + \frac{1}{\cos\theta_2}\ \varepsilon(KE_0)\right) \qquad (2.13)$$

is the stopping cross section factor in the surface energy approximation.

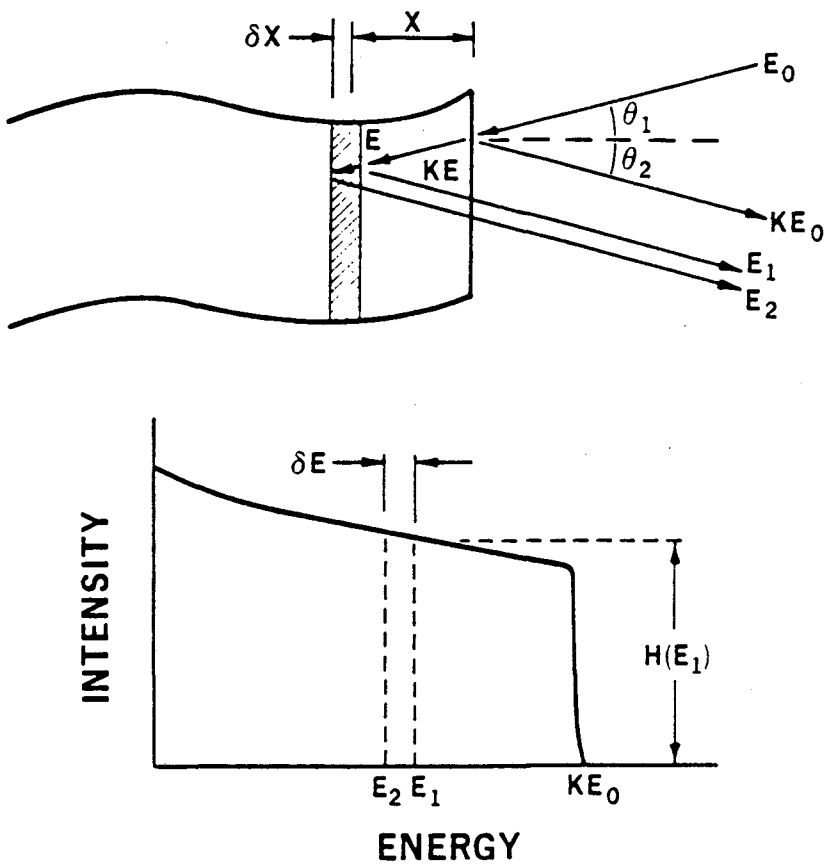

Fig. 2.4 Schematic of a backscattering process in the surface region and at a depth x of a sample consisting of a monoisotopic element(a) and the resulting energy spectrum (b).

For a thick target(>1000Å), the height of the backscattered signal in the energy spectrum can be related to the scattering

cross section σ and the stopping cross section $\varepsilon(E)$. Considering a thick sample as shown in figure 2.4, the height of the spectrum at energy E_1 is given by

$$H(E_1) = Q\sigma(E)\Omega N \frac{\delta x}{\cos\theta_1} \tag{2.14}$$

where $N\delta x$ is the amount of material in the target necessary to slow down the projectile ions by δE, the energy width of a channel in the spectrum. So we can write $N\delta x=\delta E/[\varepsilon(E)]\bullet\varepsilon(KE)/\varepsilon(E_1)$ [26]. Hence at any depth x below the surface of the target, the spectrum height $H(E_1)$ is

$$H(E_1) = Q\sigma(E)\Omega\frac{\delta E}{[\varepsilon(E)]} \frac{\varepsilon(KE)}{\varepsilon(E_1)} \tag{2.15}$$

Of particular interest is the surface yield H_0 (x=0), where $\varepsilon=[\varepsilon_0]N\delta x$ and $KE=E_1$

$$H_0 = \frac{\sigma(E_0)\delta E Q\Omega}{[\varepsilon_0]\cos\theta_1} \tag{2.16}$$

For the case of compounds, the energy loss processes are essentially the same as for pure elements. In 1905 Bragg and Kleenman postulated the principle of the additivity of stopping cross sections[31], later known as the Bragg's Rule and it was stated as follows:

$$\varepsilon^{A_mB_n} = m\varepsilon^A + n\varepsilon^B \tag{2.17}$$

where $\varepsilon^{A_mB_n}$ is the stopping cross section of the molecule A_mB_n, m and n are the atomic fraction of atoms A and B, and ε^A and ε^B are the stopping cross sections of the atomic constituents A and B. Hence the energy loss of the compound becomes

$$\left(\frac{dE}{dx}\right)^{A_mB_n} = N^{A_mB_n}\varepsilon^{A_mB_n} \tag{2.18}$$

where $N^{A_mB_n}$ is the density of the molecular units A_mB_n in the compound.

2.4 Energy Straggling and System Energy Resolution

Ideally the energy spectra obtained from an RBS experiment should have sharp, step like features as shown in figure 2.5. However, in reality, this is not the case. Deviations from ideal case are due mainly to two reasons. One is energy straggling, the other is the resolution due to the energy detection system, in particular the solid state detector itself. Energy straggling is due to the statistical fluctuations in the energy loss process when the energetic ions move through a medium. It depends on the projectile and the target atomic number and the density and thickness of the target. The Bohr value Ω_B[32] gives the approximate straggling of a target with atomic number Z_2, density N and thickness t

$$\Omega_B^2 = 4\pi(Z_1e^2)^2NZ_2t \tag{2.19}$$

In this expression, Bohr assumed that an individual energy transfer takes place between a free stationary electron and a fully ionized projectile of charge Z_1e which is only valid in the Bethe-Bloch or high energy region. This energy straggling rounds off the steps of the backscattering signals from the interfaces beneath the sample surface.

The energy resolution is due to the noise in the detector and the electronics, and to variations in the energy E_0 of the incident particles. The sum of these fluctuations can be represented approximatly by a Gaussian function with a standard deviation Ω_r. This is often defined as the system energy resolution. This system resolution results in a finite slope in the high energy edge in the energy spectrum. Since the backscattering spectra most often display the convolution of the Gaussian distribution with a step-like function, the 16 to 84% points describe these variances(figure 2.6). The convolution of the straggling and the detector energy resolution functions with the ideal spectrum (figure 2.5) results in a spectrum as shown in figure 2.7. The total effect is written as Ω_{s+r}, which is given by

$$\Omega_{s+r}^2 = \Omega_s^2 + \Omega_r^2 \qquad (2.20)$$

The system resolution can always be estimated from the high energy edge of the monoisotopic target and the energy straggling from the low energy edge by equation 2.20.

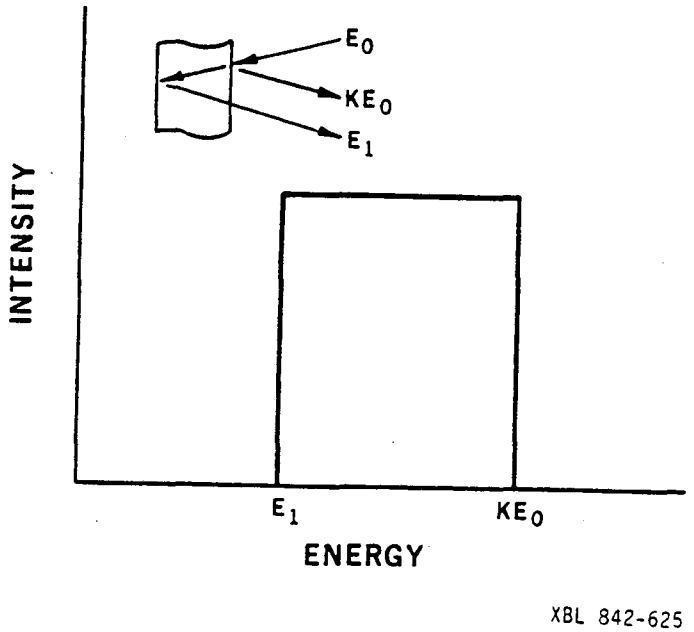

Fig. 2.5 Ideal backscattering energy spectrum for a thin film sample.

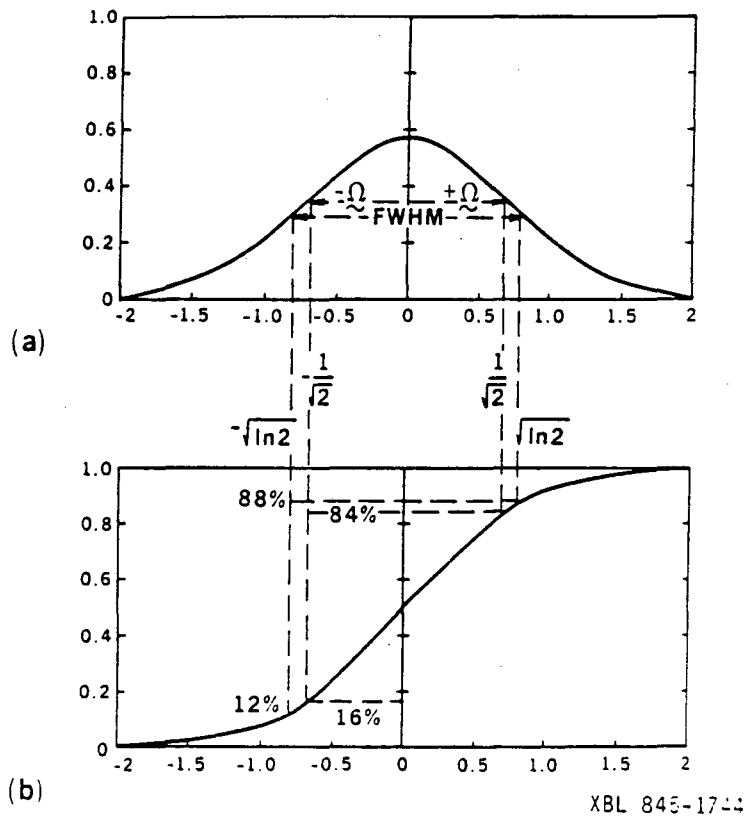

Fig. 2.6 (a) the Gaussian distribution $(2\pi\Omega^2)^{-1/2}\exp[-(x^2/2\Omega^2)]$ with $\Omega=1/\sqrt{2}$, and (b) the corresponding error function integral $\mathrm{erf}(x)=(2\pi\,\Omega^2)^{-1/2}\int_{-\infty}^{x}\exp[-(x^2/2\,\Omega^2)]dx$ with $\Omega=1/\sqrt{2}$.

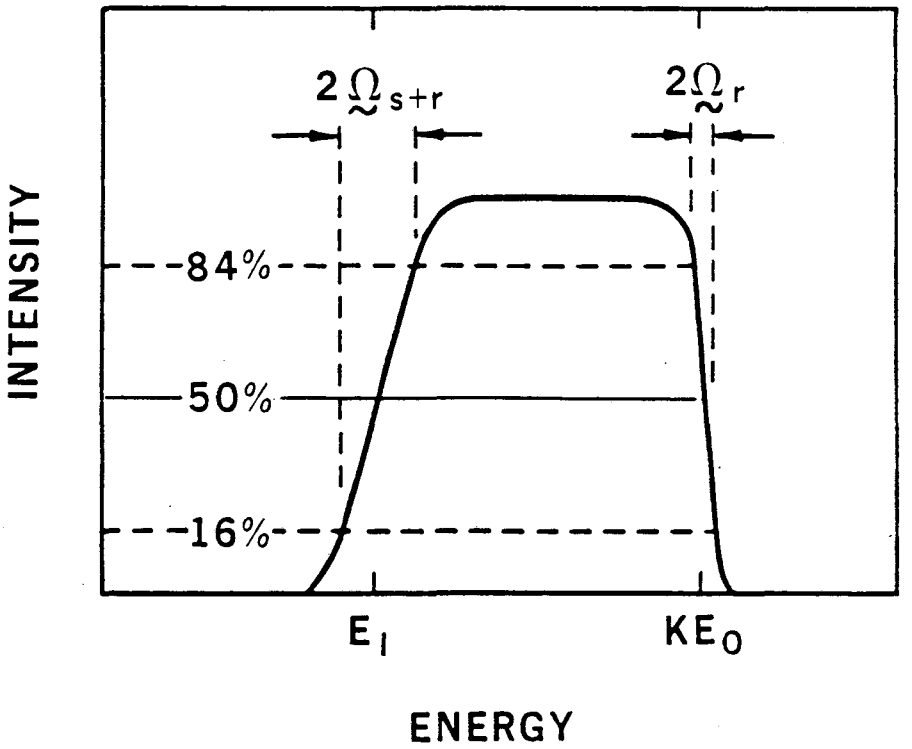

XBL 843-945

Fig. 2.7 Backscattering spectrum of a thin film sample modified by system resolution and energy straggling.

2.5 Mass Resolution and Depth Resolution

One of the most important parameter in RBS is mass resolution which can be defined as the corresponding target mass difference ΔM_2 for a system energy resolution ΔE_1(FWHM) at a certain back-scattering angle θ :

$$\Delta M_2 = \frac{\Delta E_1}{E_0 (dK/dM_2)} \qquad (2.21)$$

In section 2.1, it has already been pointed out that K, the kinematic factor is most sensitive to change in M_2 at $\theta=180^\circ$. Therefore at 180° scattering geometry,

$$\Delta M_2 = \frac{\Delta E_1}{E_0} \frac{(M_1 + M_2)^3}{4M_1(M_2 - M_1)} \tag{2.22}$$

is a minimum.

In addition to mass resolution, depth resolution in RBS is also of great importance. Depth resolution is defined as the ability to sense compositional changes with depth or variations in impurity distributions with depth. The uncertainty in the absolute depth resolving power of the method arises from the system energy resolution. The depth resolution δx is thus expressed as

$$\delta x = \frac{\Delta E_1}{[S_0]} \tag{2.23}$$

From equation 2.23 it is obvious that in order to achieve good depth resolution, one should try to maximize $[S_0]$ and minimize ΔE_1. Not much can be done about ΔE_1 since it is limited mainly by the detector resolution, but $[S_0]$ can be changed by varying the incident and scattering angle of the beam with respect to the target surface normal (see equation 2.9). For a Si substrate, for example, depth resolution for a 2.0MeV $^4He^+$ beam scattering at $\theta_1=0^\circ$, $\theta_2=10^\circ$ and $\Delta E_1=15$keV is ≈320Å. However, the depth resolution can be improved by a factor of four by tilting the sample to a condition with $\theta_1=85^\circ$ and $\theta_2=78^\circ$.

3 CONVENTIONAL RUTHERFORD BACKSCATTERING SPECTROMETRY (α-RBS)

3.1 Introduction

The use of RBS as an analytical material characterization technique can be traced back to the 1950s [25]. One of the the most famous RBS experiment performed in 1967 was the Surveyor 5 alpha-scattering experiment [33,34]. In this experiment, the chemical composition of the lunar surface material was determined by RBS. Although the analysis was limited to the outer few microns of the lunar surface, the results agreed well with later experiments performed on lunar soil.

In the semiconductor industry, where surface layer characterization of materials is extremely important, RBS with MeV ^4He has become a very useful tool in the recent years. Its capability of microanalytical depth profiling without sample erosion makes it an ideal tool for the investigations of ion-implantation profiles, thin films deposition and reactions used for Schottky barriers and contact formation, etc.

There are several reasons for the choice of MeV ^4He ions(α particles) as projectiles, namely the availability of small accelerators such as the Van de Graaff accelerators which can produce light ion beams such as H^+ and $^4He^+$ in the MeV range, and the wide range of impurity detection(M_2>4AMU) with ^4He projectiles. Moreover, parameters for ^4He ion beams such as the stopping cross sections in different material and scattering cross

section are well established.

Figure 3.1 shows a plot of the kinematic factor as a function of the target mass for ^{4}He backscattering at θ=170°. Note that the slope of the curve approaches zero as M_2 increases. In fact, K is rather insensitive to changes in M_2 as M_2>60AMU.

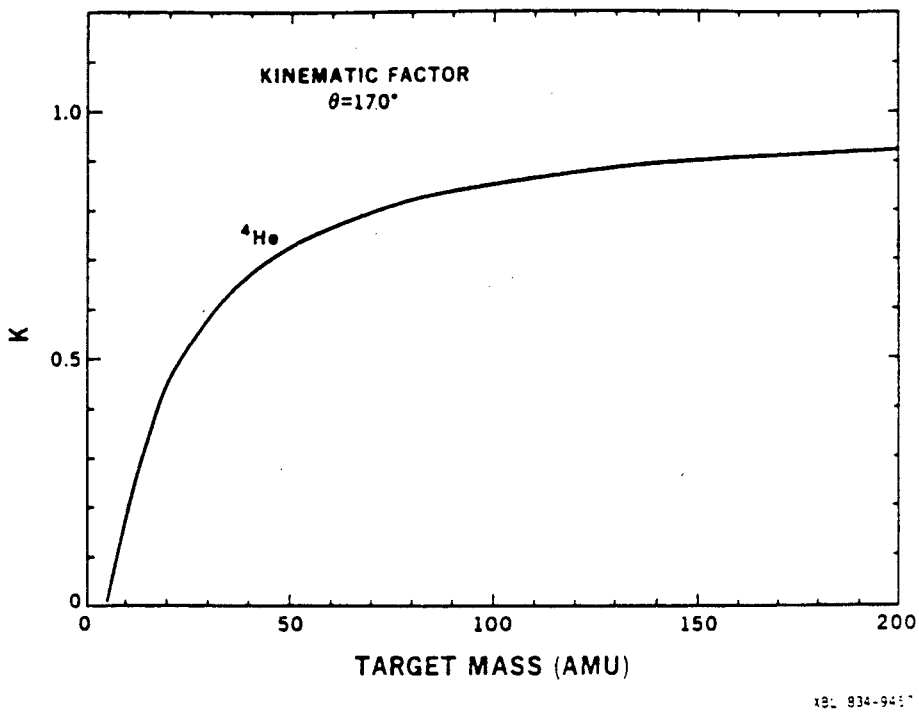

Fig. 3.1 Kinematic factor vs. target mass for ^{4}He projectiles calculated for 170° scattering angle

According to equation 2.21, mass resolution is dependent on the energy resolution of the system. For α-RBS the main contribution to the system resolution is from the detector energy resolution. Energy straggling for α particles in thin films is relatively small and can be approximated by the Bohr value given in equation 2.19. Figure 3.2 shows a plot of ΔM_2 versus M_2 for 1.5MeV ^{4}He backscattering at 180° assuming a ΔE_1 of 20keV.

Adjacent mass can be resolved for target mass $M_2<40$AMU. For heavy target elements, say Au(M=197AMU) mass resolution is poor ($\Delta M_2 \approx 20$AMU).

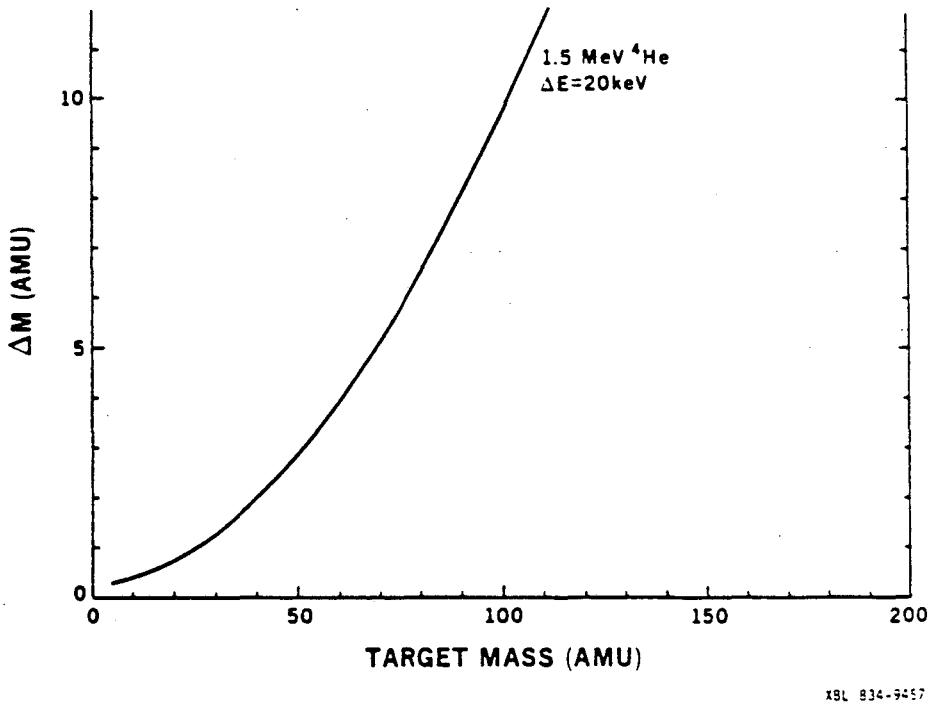

Fig. 3.2 Mass resolution vs. target mass for 1.5 MeV ^{4}He projectiles. Energy resolution of the system is assumed to be 20keV.

3.2 Examples of Analysis

3.2.1 Thin Films Studies

One of the most important applications of RBS is the area of thin films and layered structures. During the recent years, α-RBS has been used extensively in the studies of thin film interactions, interdiffusion, compounds formation, in particular the formation of metal silicides .

A schematic of the backscattering process of a thin film on a substrate and its corresponding energy spectrum are shown in

figure 3.3. Here $M'_2 > M_2$ and the thickness of the thin film t with mass M'_2 can be easily determined from the energy difference at edges 1 and 2 and the energy loss characteristics of the projectile ion M_1 in M'_2, using equation 2.7 and 2.8, we found that

$$t = (E_1 - E_2)\left(K_{M'_2}\frac{dE}{dx}\Big]^{M'_2}_{in} + \frac{1}{\cos\theta_2}\frac{dE}{dx}\Big]^{M'_2}_{out}\right)^{-1} \qquad (3.1)$$

where K'_{M_2} is the scattering factor for M'_2 and $dE/dx]^{M'_2}_{in}$ and $dE/dx]^{M'_2}_{out}$ are the energy loss along the in and out paths for M_1 in M'_2 respectively. This thickness can also be determined by measuring the energy shift of the substrate surface signal with and without the film on top. The dotted spectrum in figure 3.3(b) represents the spectrum of M_2 without the film. The thickness of the film M'_2 can therefore be expressed using the surface energy approximation, as

$$t = (E_{3'} - E_3)\left(K_{M'_2}\frac{dE}{dx}\Big]^{M'_2}_{E_0} + \frac{1}{\cos\theta_2}\frac{dE}{dx}\Big]^{M'_2}_{K_{M_2}E_0}\right)^{-1}. \qquad (3.2)$$

Figure 3.4[35] shows an example of a layer of anodically grown Ta oxide on Tantalum analyzed with 2MeV α particles. The reduced Ta concentration in the oxide layer created a step in the backscattered spectrum. From the width of this step, one can determine the thickness of the oxide layer. In addition to the thickness measurement, the composition of the oxide can also

be determined from the height of the step. Although the oxygen signal is completely masked in the substrate signal, the atomic ratio of Ta:O can still be determined by the relative heights at the interface of the Ta oxide and the Ta substrate [36].

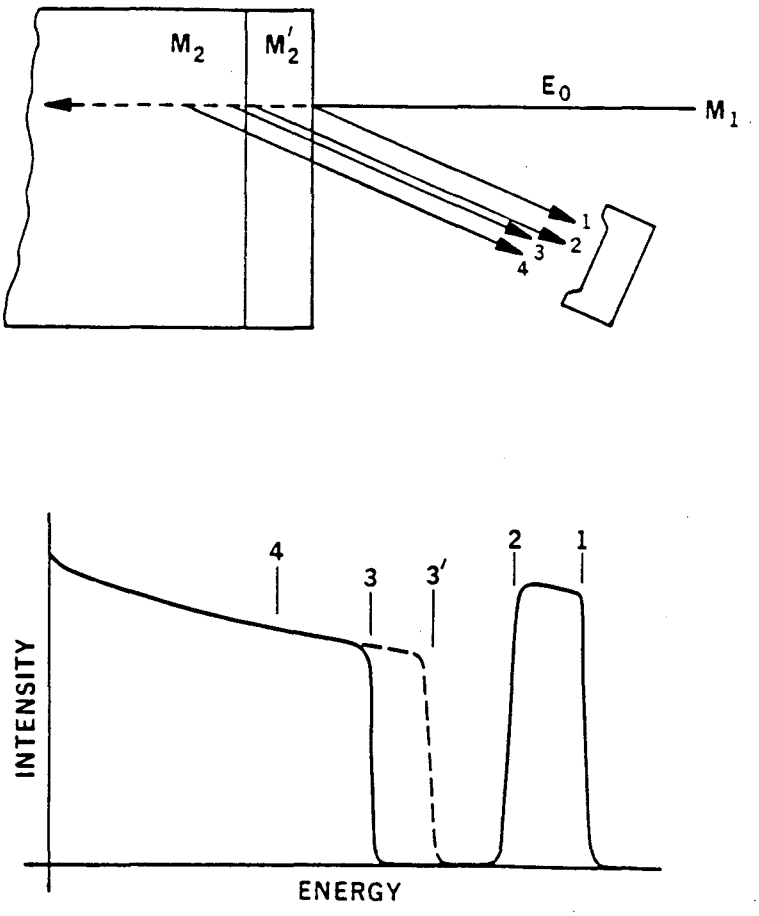

XBL 834-9455

Fig. 3.3 (a) Schematic of the backscattering process of a thin film of mass M'_2 on a substrate with mass M_2 where $M'_2 > M_2$.
(b) The corresponding energy spectrum of (a), the dotted line represents the edge of the substrate without the overlay.

In recent years metal silicides have been widely used for reliable contacts and reproducible Schottky barriers in integrated circuit applications. They are also used in power devices

such as high voltage rectifiers and thyristors. The study of the formation kinetics of silicides have been carried out primarily with α-RBS together with other techniques such as X-ray diffraction, TEM, etc. These studies involve the characterization of the reaction between two solid phases in direct contact to form ordered intermetallic compounds at temperatures well below any liquid phase.

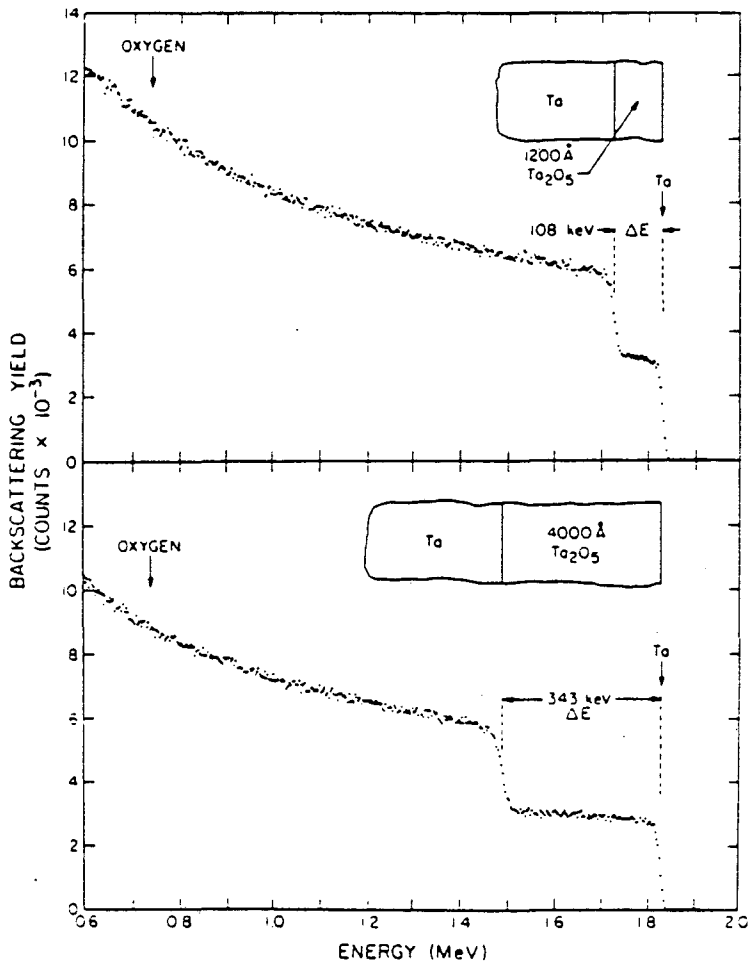

Fig. 3.4 Backscattering spectra for 2MeV ^4He ions incident on different thickness of Ta_2O_5 on Ta(Ref.35).

Figure 3.5 [37] shows an example of the characterization of

a metal silicide formation using α-RBS. In this case, the back-scattered spectra of a Ni/Si system annealed at 250°C for different times are shown. In these spectra, one can measure the energy width of the nickel silicide phase to determine its thickness while the ratio of the spectrum heights in the Ni and Si signals gives the composition ratio of the two elements in the compound formed. Moreover, one can also look at the compound formation kinetics as a function of time.

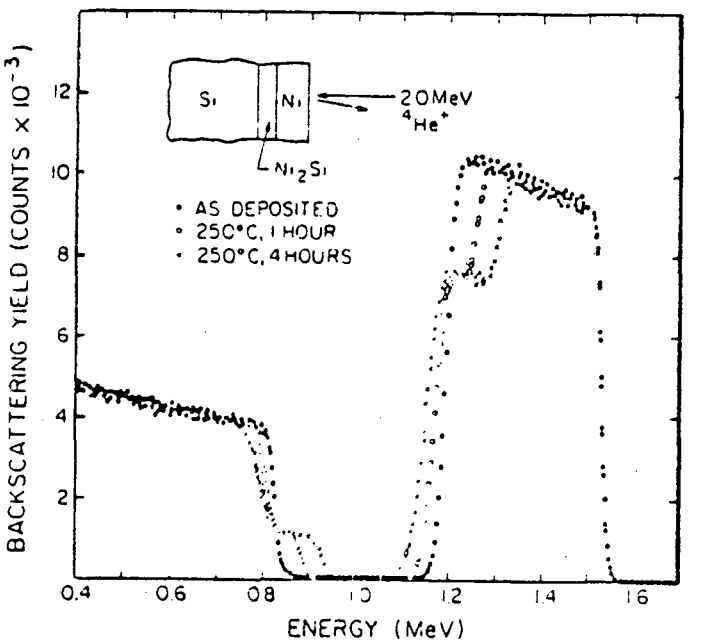

Fig. 3.5 α-RBS spectra of a sample of 2000Å Ni on (100) Si before and after heat treatment at 250°C for 1 hour and 4 hours(Ref. 37).

The study of metal silicides with α-RBS is always accompanied with a complimentary technique such as X-ray diffraction and transmission electron microscopy(TEM) for phases identification and microstructure analysis. However, α-RBS is still the easiest (in terms of sample preparation), fastest and most informative technique to use in order to obtain quantitative information on

film thickness and atomic ratios as a function of annealing time and temperature for these systems.

Thin-film interaction and interdiffusion of metal-metal systems can also be successfully studied with α-RBS [12-15]. In these applications, RBS examines intermixing of elements independently of compound formation. It does not only provide concentration profiles but also enables one to measure the activation energies and the diffusion coefficients of diffusing species in a thin film[38].

3.2.2 Ion-Implantation Analysis

RBS provides a natural technique for the study of various aspects of ion-implantation. Ion implantation, which has seen rapid development during the past 10 years, is now the most popular technique for the doping of semiconductors. The main advantages of ion-implantation include (1) precise control over total dose, depth profile and area uniformity; (2) low temperature processing; and (3) implanted junctions that can be self-aligned to the edge of the mask[39].

RBS, very closely related to ion-implantation, offers a method of measuring the implantation dose and the range profile. Together with channeling, it can also measure the damage profile introduced by the implantation process as well as the lattice location of the implanted atoms.

In figure 3.6 an energy spectrum of a 3.0MeV ^{4}He ions backscattered from a GaAs target implanted with ^{130}Te at 400keV to a dose of 10^{16} atoms/cm^{2} is shown. The integrated area of the ^{130}Te signal can directly give the number of

^{130}Te atoms/cm^2. Using the surface energy approximation, one can express the total Te dose as

$$(Nt)_{Te} = \frac{A_{Te}}{\sigma_{Te}(E_o)\Omega Q} \tag{3.3}$$

where A_{Te} is the total counts under the Te peak in the energy spectrum. Alternatively, $(Nt)_{Te}$ can also be expressed in terms of the ratio of the total Te counts A_{Te} and the surface height of the substrate element [26]:

$$(Nt)_{Te} = \frac{A_{Te}\ \sigma_{As}(E_o)\delta E}{H_{As}\ \sigma_{Te}(E_o)\ [\varepsilon_o]_{As}^{GaAs}} \tag{3.4}$$

where $[\varepsilon]_{As}^{GaAs}$ is the stopping cross section factor of GaAs in the case when As atom is the scattering atom.

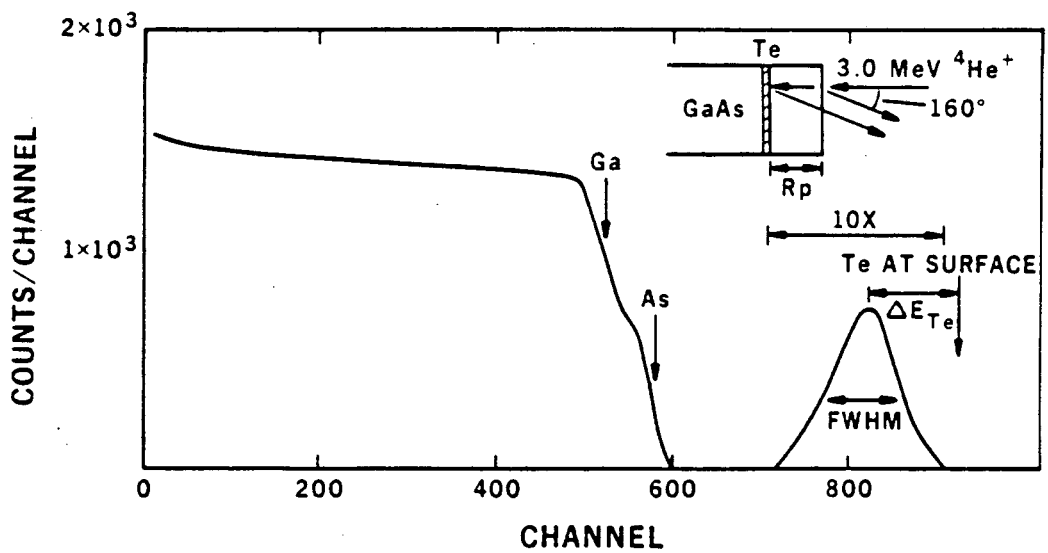

XBL 842-617

Fig. 3.6 Backscattering spectrum for 3.0MeV ^4He ions incident on a GaAs substrate implanted with ^{130}Te at 400keV to a dose of 10^{16} atoms/cm^2.

As an ion is implanted at certain energy into a substrate, it undergoes scattering events with electrons and nuclei of the substrate and loses energy until it comes to rest. According to the LSS theory[40], the distribution of the implanted ions is approximately Gaussian in shape and is described by the equation

$$N(x) = \frac{C_s}{\sqrt{2\pi}\Delta R_p} \exp[\frac{-1}{2}(\frac{x-R_p}{\Delta R_p})^2] \tag{3.5}$$

where R_p is the projected range, ΔR_p is the projected range straggling and C_s is the areal density(i.e. total dose). The projected range R_p is the average distance travelled by the energetic particles before they come to rest and the range straggling ΔR_p is the standard deviation of the Gaussian distribution in depth. The projected range is determined by the total energy shift of the Te peak from surface position ΔE_{Te} in the spectrum

$$\Delta E_{Te} = N_{GaAs}[\varepsilon_o]_{Te}^{GaAs} R_p \tag{3.6}$$

where $[\varepsilon]_{Te}^{GaAs}$ is the stopping cross section factor of GaAs with Te as the scattering atoms. The range straggling is related to the FWHM of the Gaussian Te signal by

$$\Delta R_p = \frac{FWHM}{2\sqrt{2\ln 2}N_{GaAs}[\varepsilon_o]_{Te}^{GaAs}} \tag{3.7}$$

Using the stopping cross section for ^4He in GaAs[27], R_p and ΔR_p were measured and the deviations from the tabulated values are within 5%.

In the case where the implanted dopant is much lighter than the substrate, e.g. P in GaAs, RBS is not very useful since the P signal will be completely masked in the substrate. The minimum detectable amount of implant atoms in a certain substrate depends both on the implant species and the substrate. Typically, for Te implant in GaAs, a dose of 10^{13}-10^{14} atoms/cm^2 or a peak concentration of 10^{17} to 10^{18} atoms/cm^3 is detectable with RBS.

3.2.3 Lattice Location of Impurity Atoms and Lattice Disorder Analysis

Crystallographic information of single crystals can be obtained with RBS combined with the ion-channeling technique. The channeling effect arises from the alignment of the particle beam with a major crystallographic axis of the crystal. Let us assume that a monoenergetic beam of ^4He is hitting a perfect single crystal sample. When this beam is aligned along a low index crystal direction, most of the ions (95-99% for axial channeling) are directed along the crystal channels and undergo oscillatory motion along these channels as shown in figure 3.7. These channeled ions are confined in the potential barrier formed by the atom rows or planes but they still undergo many small angle scattering events with the electrons. This multiple scattering process brings more and more channeled ions closer to the rows and planes. Since the lattice atoms are experiencing

thermal vibrations, one of these ions will come close enough to a lattice atom thermally displaced from its static rest position and it will be scattered out of the channel through large angle collision. Such process is called dechanneling. Figure 3.8 shows spectra of a beam incident along a low index crystallographic axis and along a random direction. One can see the drastic decrease in the backscattering yield for the channeled case.

The two most important parameters in ion channeling are the minimum yield χ_{min} and the half angle $\psi_{1/2}$. These are shown in figure 3.9, an angular yield profile measured in the near surface region. χ_{min} is the ratio H_A/H of the heights of the two spectra taken in the near surface region for aligned and random orientation. $\psi_{1/2}$ is the angular half width of the yield profile at the yield value half way between the minimum yield χ_{min} and the yield for the random case.

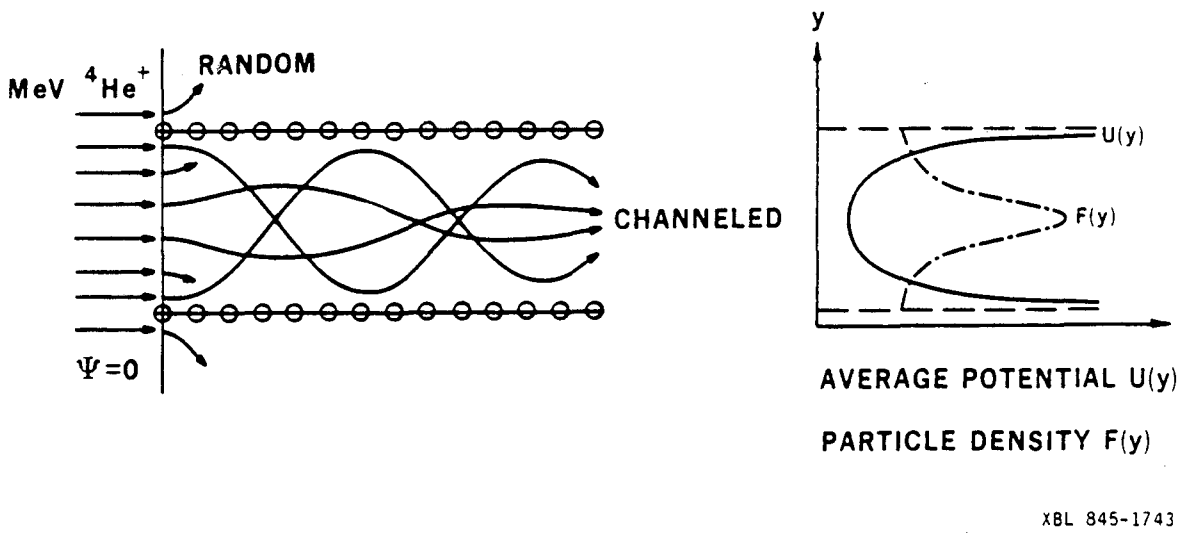

Fig. 3.7 Schematic of channeling in a crystal with plot of representative average potential and particle density across the channel.

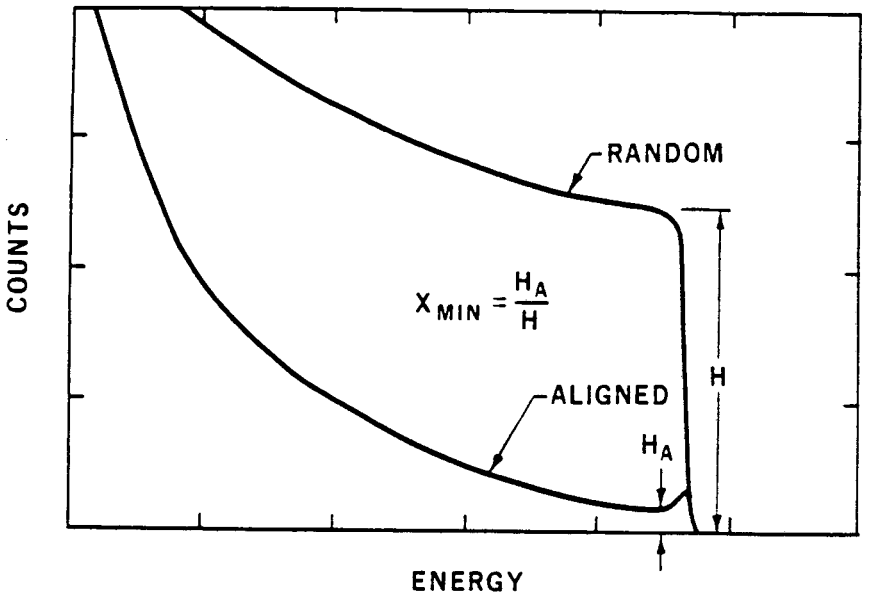

XBL 843-944

Fig. 3.8 RBS spectra of a beam incident along a low index crystallographic axis and along a random direction.

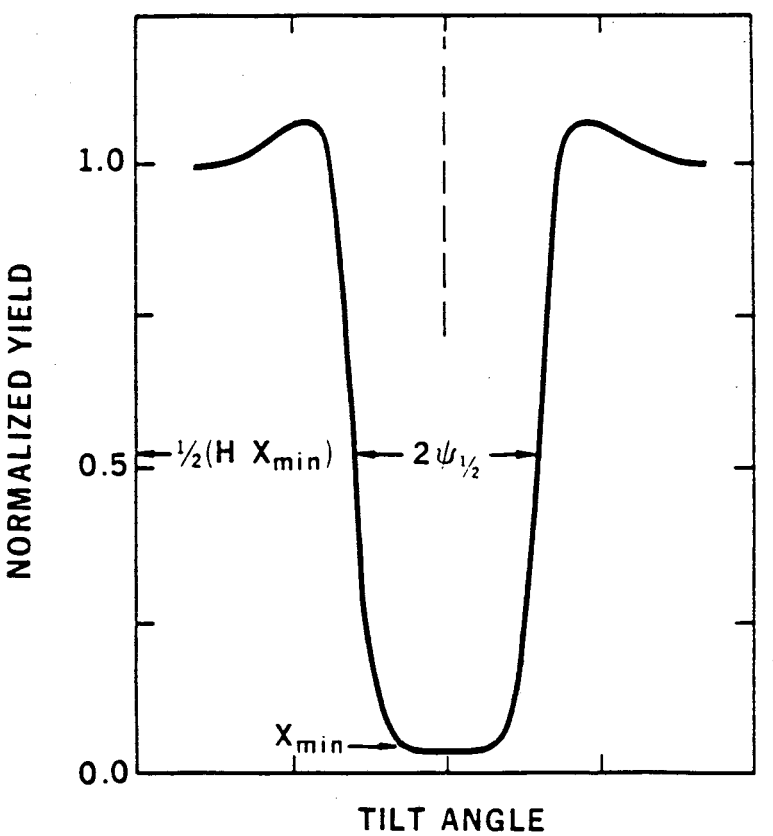

XBL 843-947

Fig. 3.9 Normalized angular yield profile measured in the near surface region.

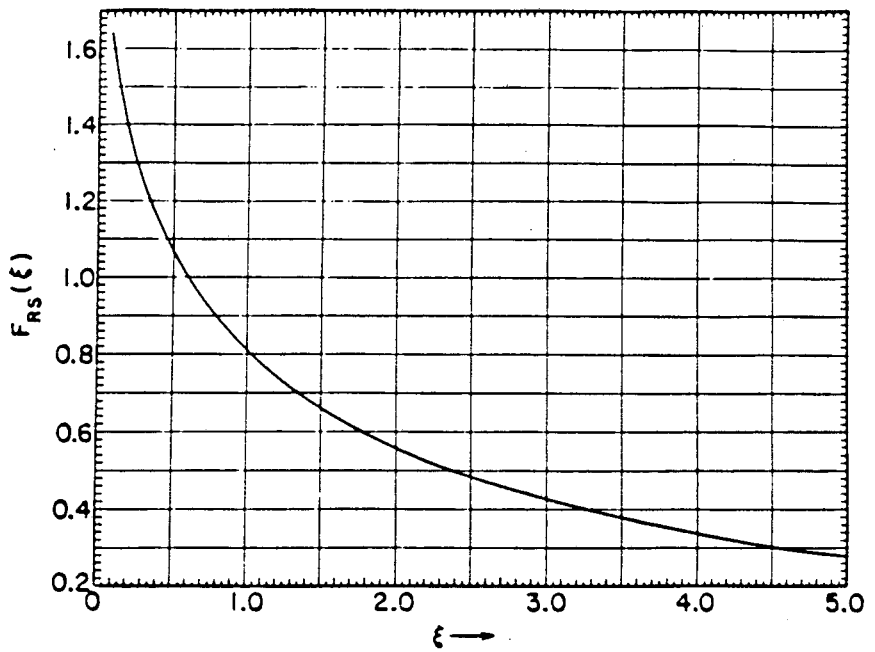

Fig. 3.10 Square root of adimensional string potential using Moliere's screening function (Ref. 41).

The values of these two parameters can be estimated from values of the Thomas-Fermi screening radius, the thermal vibration amplitude and other crystal parameters. The value of the Thomas-Fermi screening radius a is given by Barrett[41] and Gemmell[42]

$$a = \frac{0.4685}{(Z_1^{1/2}+Z_2^{1/2})^{2/3}} \quad (\text{Å}) \tag{3.8}$$

Thermal vibration amplitude u_1 and the crystal parameters are given for different materials in many books and review articles [41-44]. The half angle expressed in degree is

$$\psi_{1/2} = 0.8\ F_{RS}(\xi)\ \psi_1 \qquad (3.9)$$

where $\psi_1=0.307(Z_1Z_2/Ed)^{1/2}$ (degree) with E is the energy in MeV, d is the atomic spacing along the axial direction(in Å), and $F_{RS}(\xi)$ is the square root of the directional potential using Moliere's screening function and is shown in figure 3.10[41] with the parameter $\xi=1.2u_1/a$.

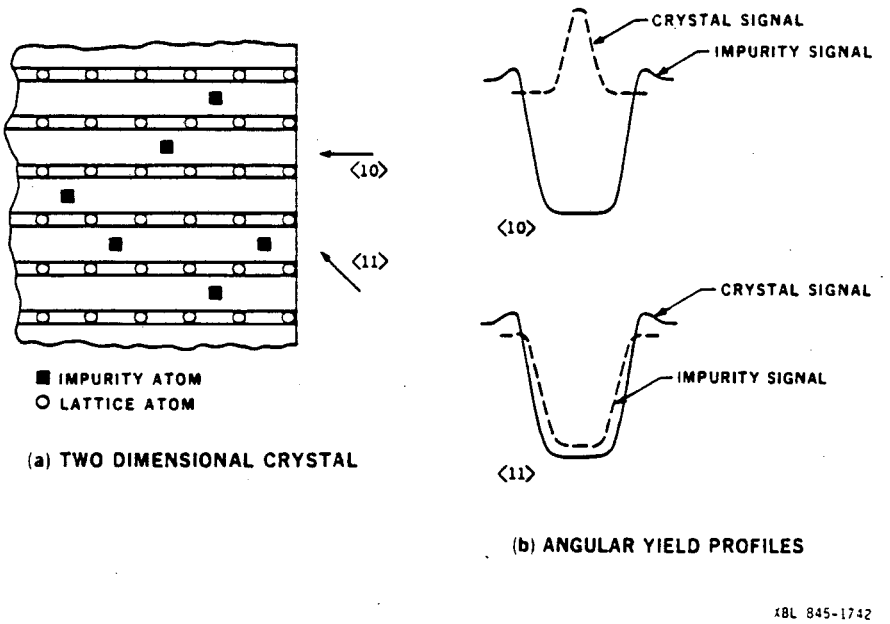

Fig. 3.11 Conceptual angular yield profiles for a two dimensional crystal.

The minimum yield for axial channeling can be estimated as [45]:

$$\chi_{min} = Nd\pi(2u_1^2 + a^2) \qquad (3.10)$$

Note that the axial minimum yield is energy independent. To

determine the lattice location of foreign atoms in a crystal, the angular yield profiles about several different axial direction must be obtained. Consider a two dimensional crystal with interstitial impurities as shown in figure 3.11(a). The corresponding angular yield profiles about two axes <10> and <11> are shown in figure 3.11(b). About the <11> axis, the yield from the interstitial atoms matches that of the host crystal since the interstitial foreign atoms lie along the <11> rows. On the other hand, along the <10> direction there is a narrow peak in the foreign atom signal due to the enhancement of the ion flux in the center of the channel. For a substitutional impurity, the angular yield profile along the <10> axis also matches that of the host lattice. For a real crystal, the problem of identifying lattice locations are more complicated but the basic concepts are still the same.

Another problem which can be analyzed by the combined method of α-RBS and ion channeling is the investigation of lattice disorder. Lattice defects such as dislocations, stacking faults, twins, etc. enhanced dechanneling. The dechanneled yield normalized to the random yield at a depth in a RBS spectrum is given by:

$$\chi_R(z) = \chi_v(z)+[1-\chi_v(z)][1-\exp(-\sigma N_D(z))] \qquad (3.11)$$

where $\chi_v(z)$ is the aligned yield for the virgin crystal, σ is the dechanneling cross section for the defects and $N_D(z)$ is the total number of defects per cm^2 integrated from the surface to depth z.

For the case of edge dislocations, channeled ion impinging normal to the dislocation line see a distorted axial or planar channel due to the bending of the atomic planes (figure 3.12 [16]). The interactions of the channeled ions with the strain field surrounding the dislocation line can be approximated in terms of a dechanneled cross section per unit length of dislocation line λ. For defects such as dislocations which involve only small total concentrations of displaced host atoms, direct scattering is negligible as compared to the dechanneling signal. Therefore the normalized aligned yield $\chi_D \simeq \chi_R$. Hence one can write [16]:

$$\frac{1-\chi_D(z)}{1-\chi_v(z)} = \exp\left[-\lambda L(z)\right] \tag{3.12}$$

where L(z) is the total length of dislocation lines/cm^2 between surface and z. It was also found theoretically by Quéré [46] that for both axial and planar channeling

$$\lambda L(z) = k(z)E^{\frac{1}{2}} \tag{3.13}$$

where k(z) is dependent upon the channeled particle and the target parameters and E is the energy of the projectile ions. Since λ is a parameter which can be calculated with reasonable accuracy, the projected dislocation density length L(z) can be estimated.

Since different defects give rise to different dechanneling factors, α-RBS/ion channeling method can, in essence, tell the

nature of different defects. However, in order to unambiguously characterize the depth profiles, nature and quantity of the defect, technique such as TEM is always used in conjunction to α-RBS/ion channeling.

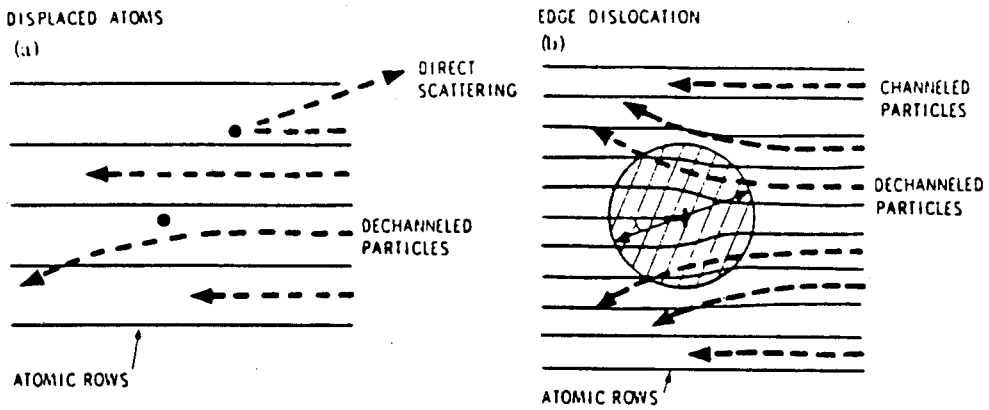

Fig. 3.12 Schematic of the processes of (a) direct scattering and dechanneling by displaced atoms and (b) dechanneling by dislocation (Ref. 46).

3.3 Limitations

Aside from the various types of problems that can be analyzed with α-RBS, there are certain basic limitations to the method. One of the most obvious one is its lack of sensitivity for low Z impurities. Because of the Z^2 dependence of the Rutherford scattering cross section, detection of low Z impurities in high Z substrates is difficult since the relatively low yield by the impurities will be covered by the high substrate signals. In the case of a single crystal substrate, the detection sensitivity can be improved by orders of magnitude by using the

channeling technique which reduces the substrate yield.

The insensitivity of the K factor with respect to changes in target masses for high Z elements puts a limitation on the applications of α-RBS to heavy materials. Figure 3.1 shows the poor mass resolution of the method at M_2>50AMU. As a consequence, analyses of the impurity profiles in ion implantation and diffusion, the analyzable depth for high Z substrates is limited. The analyzable depth of the impurity distribution refers to the maximum depth below the substrate surface from which impurity signals are still resolvable in the spectrum. Here we only consider the case where the dopant mass is greater than the substrate mass. This analyzable depth can thus be written as

$$x_{imp} = \frac{(K_{imp}-K_{sub})E_o}{[S_o]^{sub}_{imp}} \qquad (3.14)$$

where the subscripts imp and sub represent the corresponding parameters for the impurities and the substrate. Table 3.1 shows some of the calculated values for the analyzable depths for different dopants in Si and Ge substrates.

The analyzable depths given below are in μm

		Si substrate		Ge substrate	
Ion	E_o(MeV)	P	As	Se	Te
^{4}He	2.0	0.14	1.0	0.037	0.27

Table 3.1 Calculated values of analyzable depths for 2.0 MeV ^{4}He beam for the analysis of various impurities in Si and Ge.

Figure 3.13(a) shows a 3.0MeV ^{4}He RBS spectrum of 400keV ^{130}Te implanted GaAs. The Te signal is well separated from the substrate signal. Figure 3.13(b) shows another spectrum with the same beam for 800keV ^{130}Te implanted GaAs. The Te signal is completely mixed with the substrate signal. The projected range R_p for this implantation is about 1900Å and ΔR_p about 900Å.

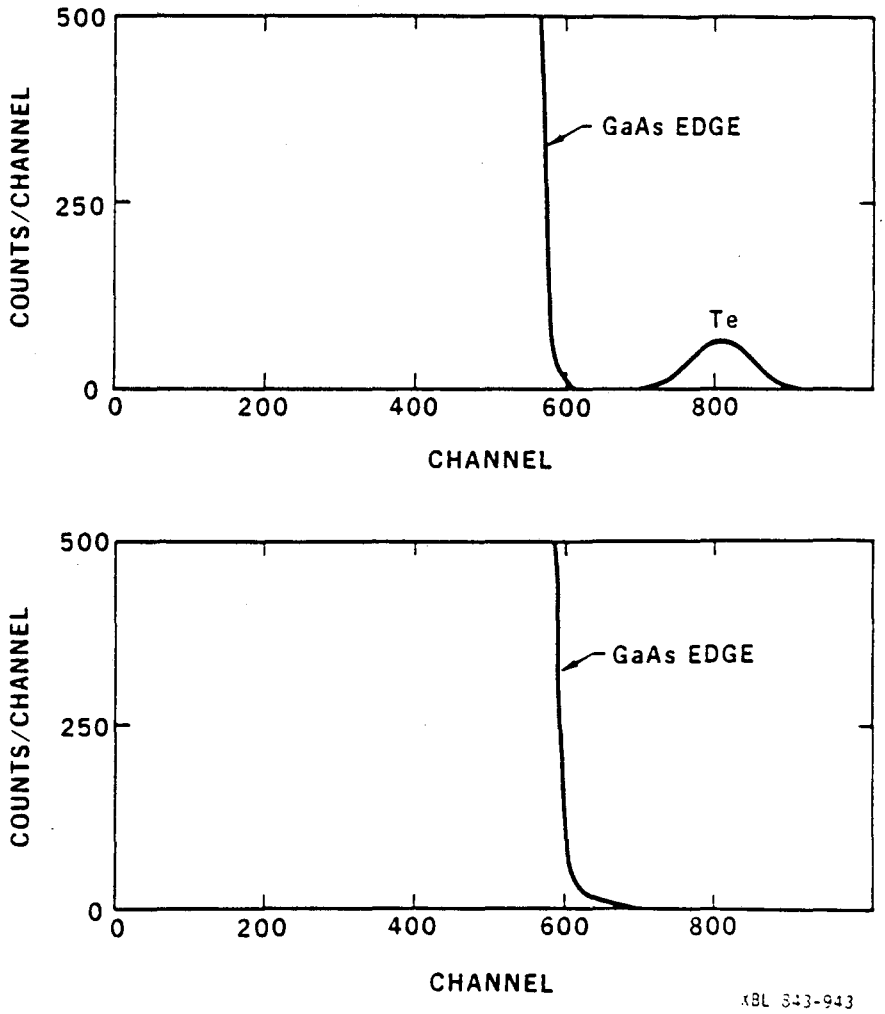

Fig. 3.13 Backscattering spectra for 3.0 MeV ^{4}He ions incident on a GaAs substrate implanted with ^{130}Te at (a) 400keV and (b) 800keV to a dose of 10^{15} atoms/cm^{2}.

The poor mass resolution of α-RBS for high Z elements also puts a limit on the study of thin films. Film thickness determination of thin films will be difficult due to signal overlapping for heavy films such as Au/Pt, Pd/Rh,etc. Study of multiple layered metallizations on heavy semiconductors with α-RBS is difficult or even impossible. Figure 3.14 shows a 1.5 ^{4}He backscattering spectrum for a typical Schottky contact for GaAs(500Å Au/500Å Pt/ 500Å Cr on GaAs).. It is impossible to resolve the Au and Pt layers which have a mass difference of 2AMU. Figure 3.15 shows th Pd_2Ge formation kinetics by RBS in a Au/Pd/Ge system. After 200°C anneal for one hour one detects diffusion of Au into the Pd and also reaction of Pd and Ge. However, because of the poor resolution, not much information about the atomic ratio of Pd and Ge in the Pd/Ge compound, the thicknesses of different layers and the Au diffusion can be deduced from the spectrum.

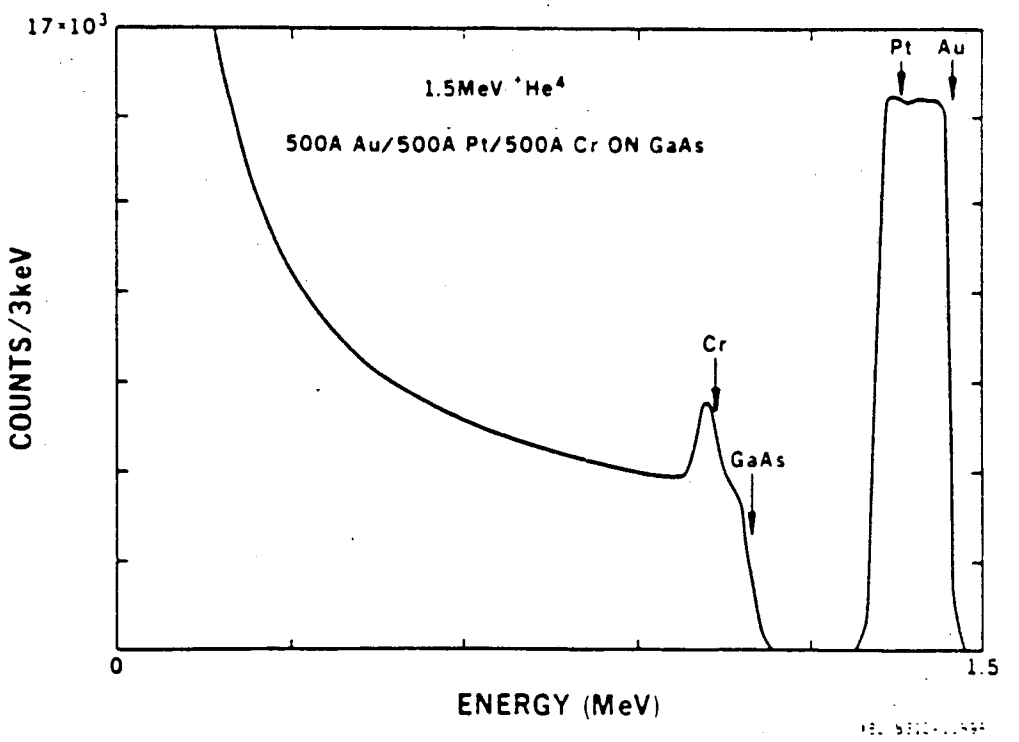

Fig. 3.14 1.5 MeV ^{4}He ion RBS spectrum for a typical Schottky contact structure for GaAs: 500Å Au/500Å Pt/500Å Cr on GaAs.

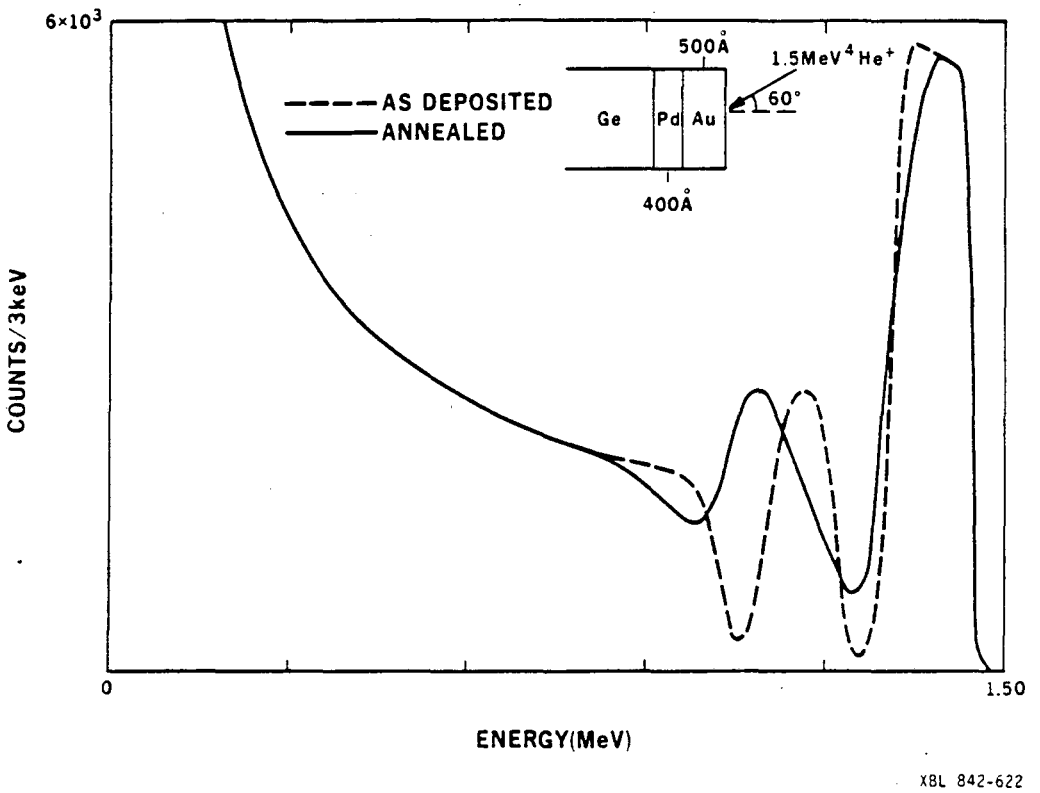

Fig. 3.15 1.5 MeV ^{4}He ion RBS spectra for a Au/Pd on Ge system as deposited (dash line) and after 200°C anneal for 1 hour (solid line).

4 HEAVY ION RUTHERFORD BACKSCATTERING SPECTROMETRY(HIRBS)

4.1 Introduction

The basic physics of HIRBS is, in essence, identical to that of RBS. The differences between the two techniques lies in the differences in the charge, mass, and energy of the projectile ions which change the parameters in the scattering experiment. Consequently, the resulting backscattering spectra in HIRBS is affected in various ways.

In order to avoid nuclear reaction between an energetic charged particle and a nucleus, the energy of the charged projectile particle must be below the Coulomb barrier caused by the electrostatic repulsion between the nuclear charge and the particle charge. In other words, the classical scattering process is valid only when the incident energy E_0 of the projectile is smaller than the Coulomb barrier. The height of this Coulomb barrier can be written as

$$E_{Coul} = \frac{Z_1 Z_2 e^2}{(R_1+R_2)} \tag{4.1}$$

where Z_1, Z_2 are the atomic numbers and R_1, R_2 the nuclear radii of the projectile ions and the target atoms. The nuclear radius is given by

$$R = r_0 A^{1/3} \tag{4.2}$$

with A the mass number and r_0 the radius parameter depending upon the type of experiment used for its determination. The values of r_0 ranges from 1.2 to 1.5 fermi(1 fermi=10^{-15}m). Hence,[47]

$$E_{Coul} = \frac{Z_1 Z_2 e^2}{r_0 (A_1^{1/3} + A_2^{1/3})} \quad . \tag{4.3}$$

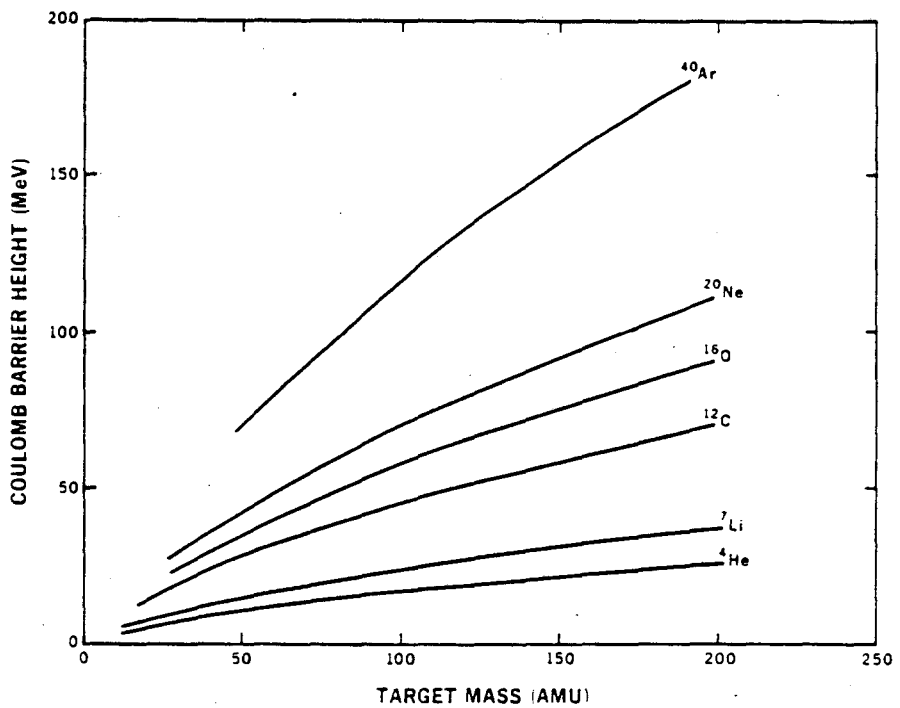

Fig. 4.1 The Coulomb barrier heights plotted as a function of target mass M_2 for different ions with masses ranging from 4 to 40AMU.

When heavy ion is used as projectiles (M_1>4AMU), the Coulomb barrier increases. While high projectile energy is preferred as far as mass resolution is concerned, heavy projectiles are of great advantage in backscattering spectrometry because high

energy can be employed with heavy projectiles without breaking the Coulomb barrier, and therefore without the interference of nuclear reactions of the projectile ions and the target elements. Figure 4.1 shows the Coulomb barriers of ^{4}He, ^{7}Li, ^{12}C, ^{16}O, ^{20}Ne beams as a function of M_2.

Figure 4.2 shows the kinematic factor K as a function of target mass M_2 for various projectile masses with scattering angle $\theta=170^{\circ}$. It is obvious that for large M_2 the slope of the curve increases as M_1 increases. The increase in sensitivity of K for heavy target masses using heavy projectiles results in the increase in mass resolving power. This is particularly important for the analysis of heavy materials.

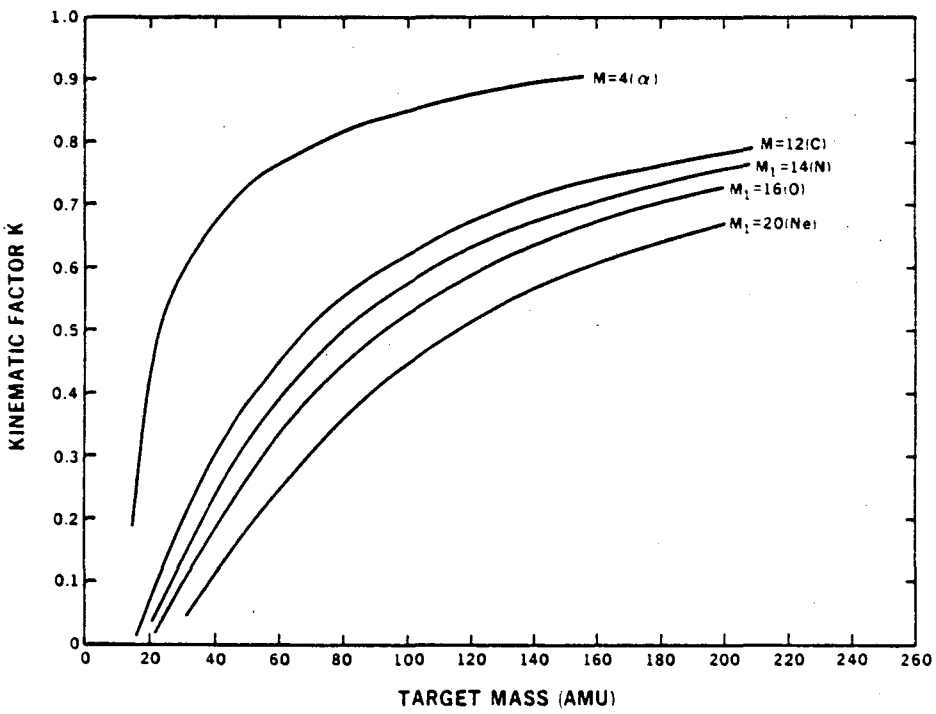

Fig. 4.2 The kinematic factor K plotted as a function of target mass M_2 for different ions with mass ranging from 4 to 20 AMU.

The energy loss characteristics for different ion beams in different materials have been well studied [27,48]. Figure 4.3 shows dE/dx as a function of projectile energy for ^4He and ^{16}O particles in Al and Ge targets. In order to achieve the best depth resolution and greatest depth penetration, it is desirable to choose the energy of the beam so that its effective energy loss $(dE/dx)/E_0$ in the material is a minimum. Therefore, it is obvious that higher incident energies should accompany heavy projectiles in order to optimize the results.

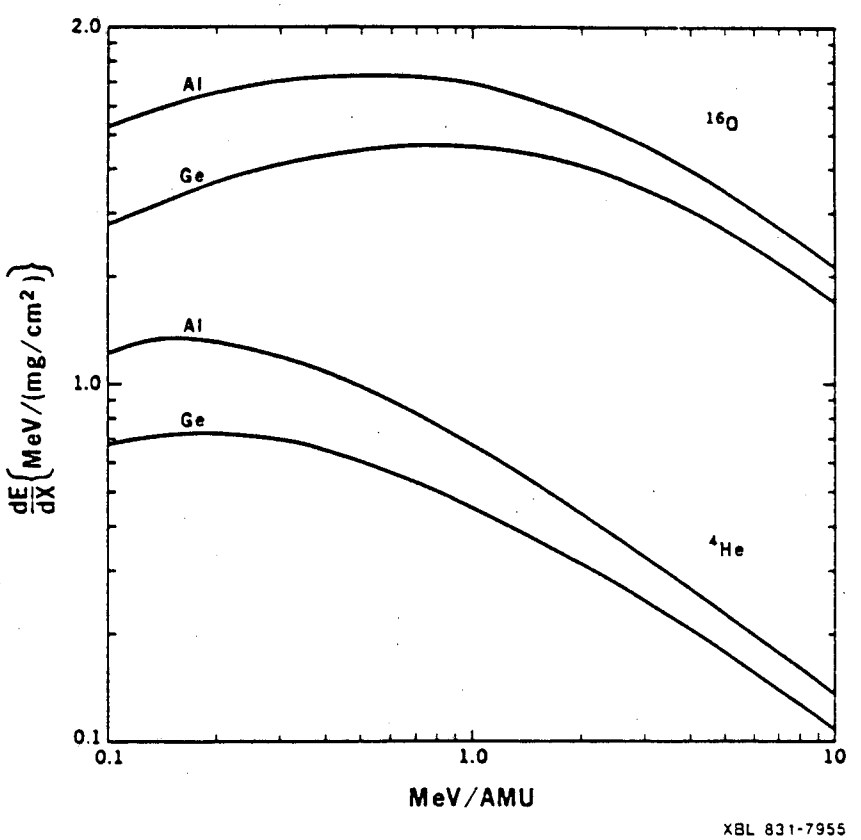

Fig. 4.3 Stopping power dE/dx of ^{16}O and ^4He particles in Al and Ge targets plotted as a function of energy/ion mass (MeV/AMU).

Furthermore, one should also look at the differential scattering cross section $d\sigma/d\Omega$. Since $d\sigma/d\Omega \sim (Z_1Z_2/E)^2$, increasing Z_1 should increase the yield significantly. However, at the same time E is increased to an even greater extent so that the net result is a decrease in the yield.

The choice of a certain ion as projectile at certain incident energy for optimum results can only be made after considering all the effects the projectile ion has on the parameters of the backscattering process. In addition to the effects mentioned above, it is also important to point out that the detector resolution worsens as the energy and the mass of the projectile increases. Finally, the use of heavy ions also results in the loss of sensitivity to any light impurities with mass $M_2<M_1$. With all these points in mind, the choice of $^{16}O^{++}$ ions with energy at 20MeV were used in the following HIRBS experiments.

4.2 Important Parameters

4.2.1. Energy Straggling

As mentioned in section 2.4, the energy straggling arises from the statistical fluctuations in the energy loss process for an energetic ion passing through a medium. It can be approximated by the Bohr value Ω_B given by equation 2.19. Considering both the inward and outward straggling, the total theoretical approximation is given by

$$\Omega = (K^2\Omega_{in}^2 + \Omega_{out}^2)^{1/2} \tag{4.4}$$

where $\Omega_{in} = (4\pi(Z_1e^2)^2NZ_2t/\cos\theta_1)^{1/2}$, and
$\Omega_{out} = (4\pi(Z_1e^2)^2NZ_2t/\cos\theta_2)^{1/2}$.

For α backscattering, the energy stragglings for films of thickness < 3000Å is of the order of a few keV and agree well with the Bohr values. However, for the case of heavy ion RBS, this type of stragglings is sometimes not negligible.

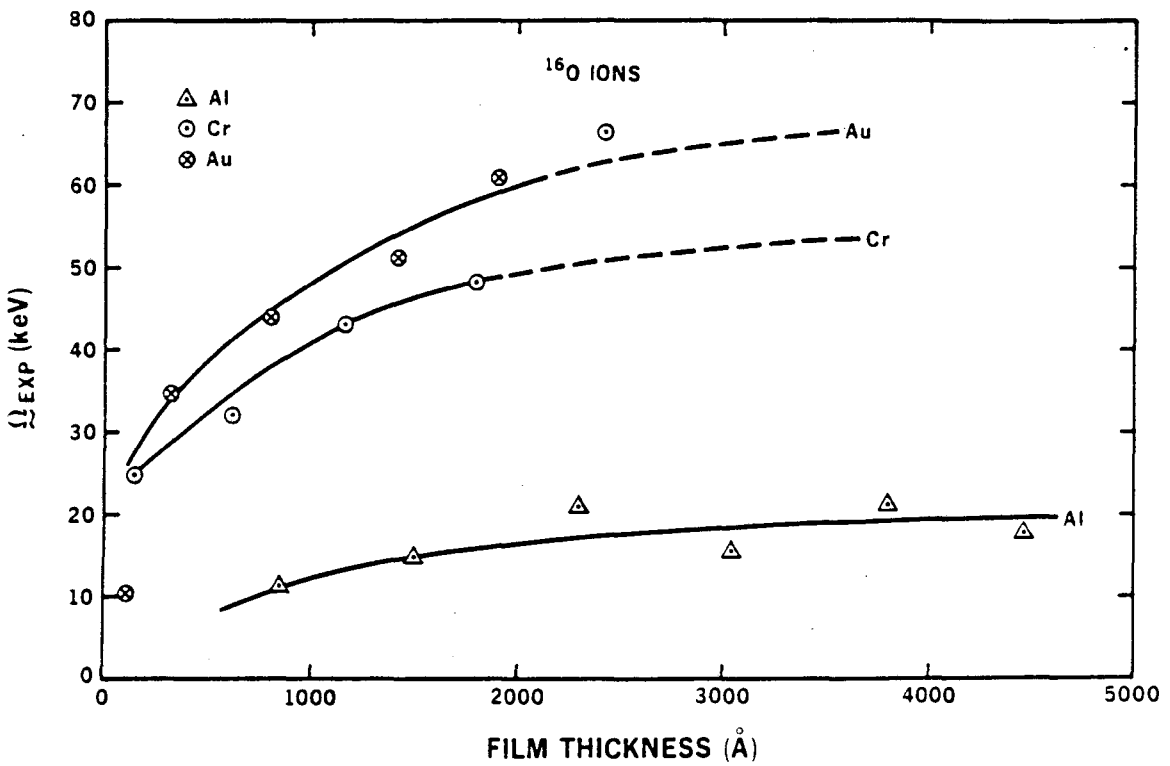

XBL 842-628

Fig. 4.4 Plots of the experimental energy stragglings as a function of film thicknes for 20 MeV ^{16}O ions in Au, Cr and Al targets.

The energy straggling for 20MeV $^{16}O^{++}$ beam in various media was studied. The metals investigated were Al, Cr, and Au. Various thicknesses of the metals were thermally deposited on Rh

substrates and the total experimental straggling were given by the FWHM/2.355 of the Rh edges in the resulting spectra. We chose to use Rh as substrates for two reasons. Firstly it is monoisotopic and the resulting RBS spectra gave a single Rh edge. This makes the data analysis easier. Secondly, the mass differences between Rh and the metals we studied are sufficiently large so that no signal overlap occurred. Figure 4.4 shows the Ω_{exp} versus film thickness for 20MeV $^{16}O^{++}$ in the three media. For a heavy medium such as Au, the straggling for films of thicknesses > 1000Å is comparable to the system resolution. Therefore, in the analysis of HIRBS results, energy straggling is not anymore negligible effects. The deviations of the experimental straggling data from the Bohr values are plotted on figure 4.5. From these curves, one can see that the experimental straggling values approach the Bohr values for thick film (>4000Å) and heavy media.

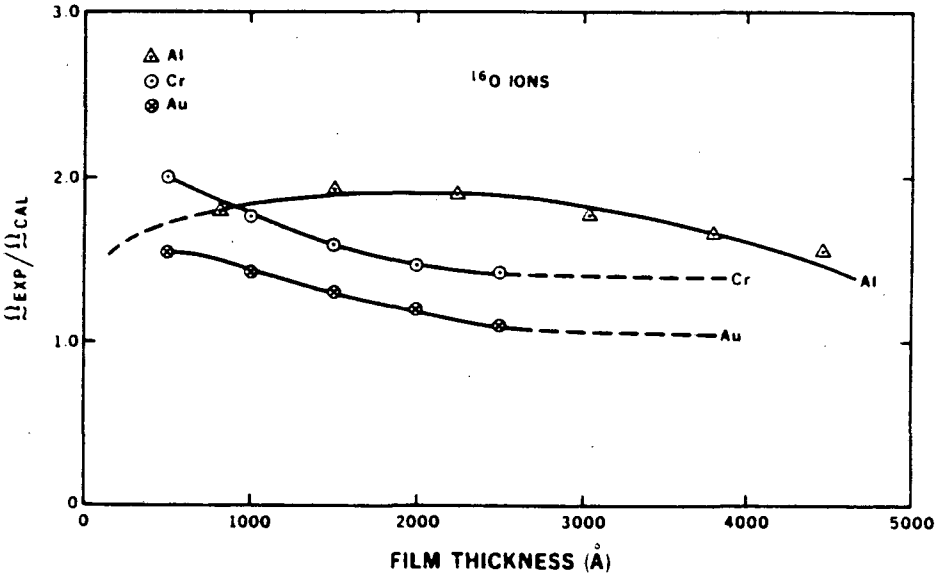

Fig 4.5 Plots of the deviations of the experimental energy straggling from the theoretical Bohr values as a function of the target film thickness for ^{16}O ions in Au, Cr and Al.

4.2.2 Energy Resolution, Mass Resolution, and Depth Resolution

The main contribution for the total energy resolution of the system is the detector resolution. For a silicon surface barrier detector, the FWHM resolution for α particles is about 15keV. However, for the detection of ^{16}O particles, the resolution is degraded. Figure 4.6 shows the energy resolution for a Si surface barrier detector for ^{4}He and ^{16}O particles [49]. The degraded detector resolution for ^{16}O ions is mainly caused by the straggling of the energy loss due to nuclear collision during the slowing down of the ^{16}O ions in the silicon detector. The FWHM detector resolution for 20MeV ^{16}O ions is about seven times worse than that for 2MeV ^{4}He and is about 100keV. Other contributions to the system energy resolution are energy spread of the beam ΔE_{beam} and the kinematic energy spread due to the geometry of the set up ΔE_k. ΔE_{beam} is about .3% for the beam produced by the 88" cyclotron at LBL and ΔE_k is estimated to be about 18keV. Therefore the total energy resolution is given by

$$\Delta E_{sys}^2 = \Delta E_{det}^2 + K^2 \Delta E_{beam}^2 + \Delta E_k^2 \ . \qquad (4.5)$$

The last two terms in the above equation are relatively unimportant.

From equation 2.21, it is obvious that in order to improve the mass resolution (or reduce ΔM_2), one must:

(i) reduce ΔE_{sys},

(ii) increase E_o, or

(iii) increase dK/dM_2.

(ii) and (iii) are achieved by using 20MeV ^{16}O beam instead of a 2MeV ^{4}He beam. However, at the same time ΔE_{sys} is increased by a factor of seven. The overall improvement on the mass resolution of HIRBS is clearly illustrated in figure 4.7. Here one can see that for target mass of 100AMU, the improvement on mass resolution is about a factor of six over α-RBS.

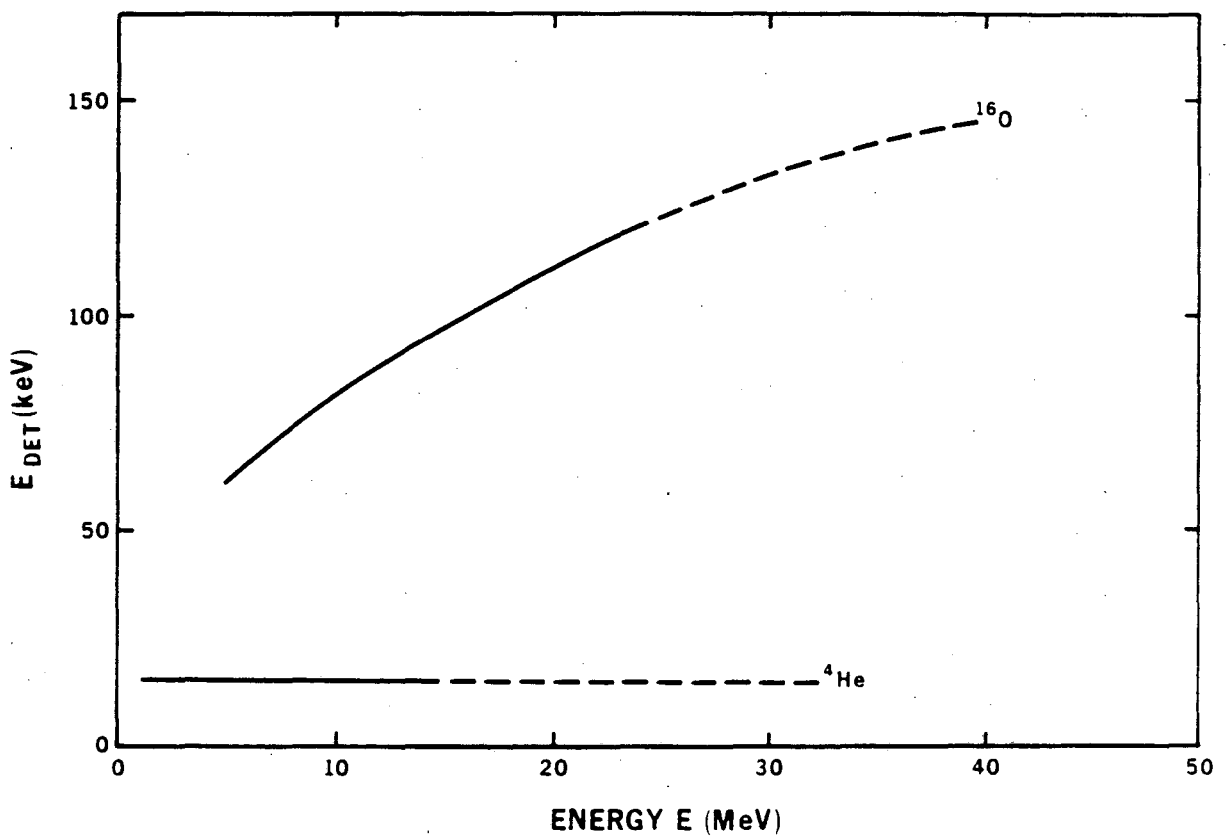

Fig. 4.6 Detector energy resolution plotted against ion energy for ^{16}O and ^{4}He ions for a Si surface barrier detector.

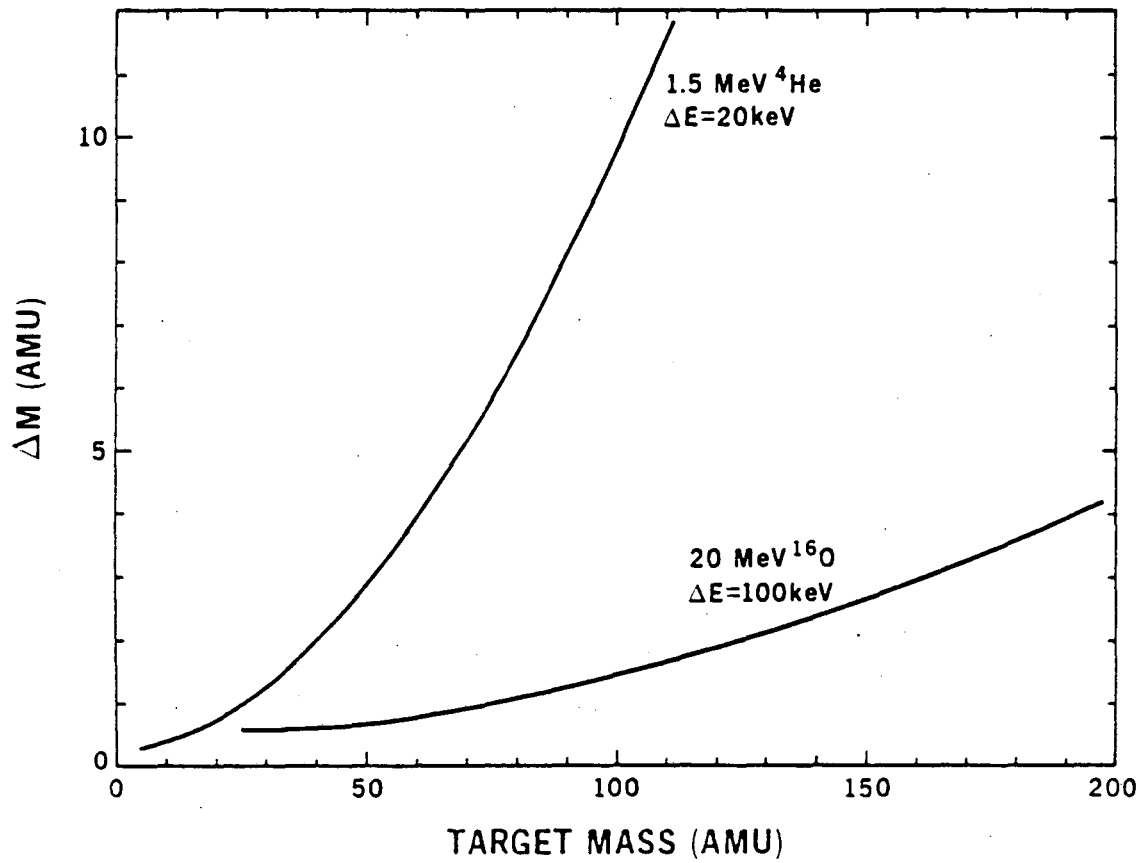

XBL 831-7958

Fig. 4.7 Calculated curves of mass resolution vs. target mass for ^{4}He and ^{16}O assuming ΔE_{sys}=20keV for ^{4}He and 100keV for ^{16}O.

The comparison on the depth resolution between conventional RBS and HIRBS is difficult because it varies with different targets. But in general, due to the degrading ΔE_{sys} in HIRBS, its depth resolution is worse than that for RBS. For heavy target elements such as Au the depth resolutions for the two cases are comparable. Table 4.1 shows a comparison of the depth resolution for 20MeV ^{16}O HIRBS and 2MeV ^{4}He RBS. ΔE_{sys} is assumed to be 100keV in the first case and 15keV for the latter case.

Depth Resolution in A

	20MeV ^{16}O	2MeV ^{4}He
Al	680	330
Ni	170	130
Pd	150	110
Ag	160	140
Au	120	110

Table 4.1 Depth resolution for 20MeV ^{16}O and 2MeV ^{4}He beams in various targets. The surface energy approximation is used in the calculation of dE/dx.

The slightly worsened depth resolution for HIRBS, however, is not a great disadvantage for the method. It has been shown in section 2.5 that depth resolution can always be improved by increasing the effective energy loss of the system through sample tilting.

4.3 Instrumentation

The technical aspects of RBS and HIRBS are essentially the same except for the fact that they use different accelerators. For α-RBS, the most widely used is the Van de Graaff accelerator.

Others which can be used to produce ^4He beams for RBS include Pelletron and Tandem. For HIRBS, big accelerators must be used to produce high energy heavy ion beams. The 88" cyclotron in LBL was used in our case. For RBS obtained here as comparison to the HIRBS results, the 2MeV Van de Graaff accelerator was used.

The energy detection systems are the same for RBS and HIRBS. A Si surface barrier detector was used in the HIRBS as well as the RBS experiments. Semiconductor detectors are used instead of gas filled detectors or scintillation counters because they have superior energy resolution, compact size, relatively fast timing characteristics, and an effective thickness which can be varied to match requirements of the application.

A semiconductor detector can be conceived as a solid state ionization chamber. It is basically a large Si or Ge diode of the p-n , p-i-n or Schottky type operated in the reverse bias mode. When a potential is applied to the electrodes of the diode an internal electric field is produced. As an energetic charged particle (or other radiation) passes through the semiconductor, many electron-hole pairs along the track of the particle are produced. These free charge carriers are then swept to the contacts by the internal electric field. Therefore the energy absorbed from the charge paritcle or radiation can be measured by measuring the current flow in the external circuit of the detector or more commonly the total charge collected on the contacts. The average energy needed to produce an electron-hole pair is called the ionization energy ε. The value of ε for

Si is about 3.8eV and for Ge is about 3eV. This ionization energy value, small compared to other detectors such as gas ionization chambers, results in a large number of charge carriers for a given energy deposited in the detector. This is of prime importance to the energy resolution because the statistical fluctuation in the number of carriers per pulse becomes a smaller fraction of the total as the number is increased. Moreover, the greater amount of charge per pulse leads to a better signal to noise ratio.

Theoretical variance in the number of electron-hole pairs (n) is

$$\langle n_0 \rangle^2 = F \langle n \rangle^2 \qquad (4.6)$$

where F is the Fano factor which is introduced in order to modify the Poisson distribution of coupled processes of charge carrier formation($F \sim 0.1$ for Si and Ge). The small F value for semiconductor detectors also contributes to their better energy resolution.

In our RBS and HIRBS experiments, a silicon surface barrier detector was used. The basic structure for a p-Si surface barrier detector is shown in figure 4.8[50]. Typically a surface barrier detector is a diode with very thin evaporated Au($40\mu g/cm^2$) contact on an etched n-type Si wafer. The Au evaporation forms the front rectifying contact of the diode, and the rear ohmic contact is composed of $40\mu g/cm^2$ of evaporated Al. When a reverse bias voltage is applied to the diode, an

electric field $\mathcal{E}$ is created:

$$\mathcal{E}(x) = \frac{2V}{W^2}(W-x) \tag{3.7}$$

where W is the depletion region width and V is the bias voltage. When W is equal to the detector thickness L, the detector is totally depleted. Only the charge carriers created by the ionization process due to the radiation in the depletion region are efficiently collected. The depletion region is therefore also called the sensitive region.

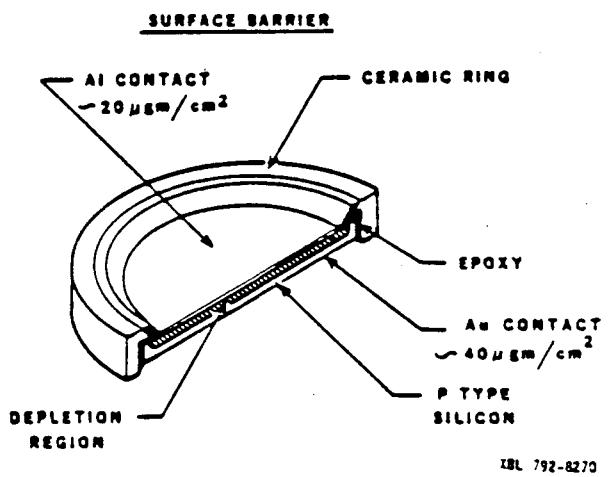

Fig. 4.8 Mechanical details of surface barrier detector fabrication

Before a charged particle or radiation reaches the sensitive region, it has to pass one or more "dead" regions. The total thickness of these "dead" regions include the metallic electrode and a layer of Si immediately beneath the electrode in which

charge collection is inefficient. For heavy charged particles, this energy loss can be significant. Therefore for HIRBS experiments it is preferable to use a surface barrier detector which has a thinner "dead" layer compared to other semiconductor detectors such as the diffuse junction type and the ion implanted detectors. Because of the thin entrance windows the surface barrier detectors are optically transparent and light sensitive. Photons striking the detector surface can reach the active volume. Hence, the experiments must be carried out in the dark.

The main problem in the use of semiconductor detectors in HIRBS is the radiation damage in the Si produced after prolonged exposure of the detector to ^{16}O particles. Radiation of sufficient energy can displace Si atoms from their equilibrium sites to interstitial positions resulting in a vacancy-interstitial complexes or it can produce large defect regions acting as carrier trapping sites. These traps reduce the carrier lifetime and degrade the energy resolution of the detector. The severity of the damage is a strong function of the nature and quantity of the radiation involved. Damage is relatively insignificant for conventional RBS experiments with 1.5 to 2.0 MeV ^{4}He ions. For HIRBS, significant degradation in the detector energy resolution (40%) was observed after 50 hours of operation with 20MeV $^{16}O^{++}$ ions at a current of ≈40 nA. This corresponds to a total number of about 200 sample analyses and is therefore considered a minor problem.

4.4 Applications (Experimental Results)

Applications of HIRBS are concentrated on medium to high Z semiconductors including GaAs, GaP, InP and Ge. Studies on different systems in different areas of semiconductor research were carried out. All of these experiments were performed using the LBL 2MeV Van de Graaff facility ($^{4}He^{+}$ at 1.5 MeV) for comparisons and the heavy ion capability of the 88" cyclotron ($^{16}O^{++}$ at 20MeV) for HIRBS. A Si surface barrier detector depleted to a depth of 200μm and with 20keV FWHM energy resolution for 5MeV α were used. Another annular Si surface barrier detector was used in some of the measurements in order to improve the count rates of the experiments without affecting the kinematics.

The particle beam size on target was 1.5mm in diameter with about 1° angular spread. The scattering angles were 170° for the conventional detector geometry and 176.6° for the annular detector with detection solid angles of 2.7msr and 16.45msr for the two detectors respectively. Total charges accumulated varied from 100-400μC for the ion implantation study and 40-80μC for the other systems. Typical vacuum achieved in the scattering chamber was of the order of magnitude 10^{-6} torr. Pulse height data were accumulated in a Davidson 1024 channel analyzer and stored on computor cassette tape for subsequent plotting and analysis. The simplified schematic of the experimental set up is shown in figure 4.9.

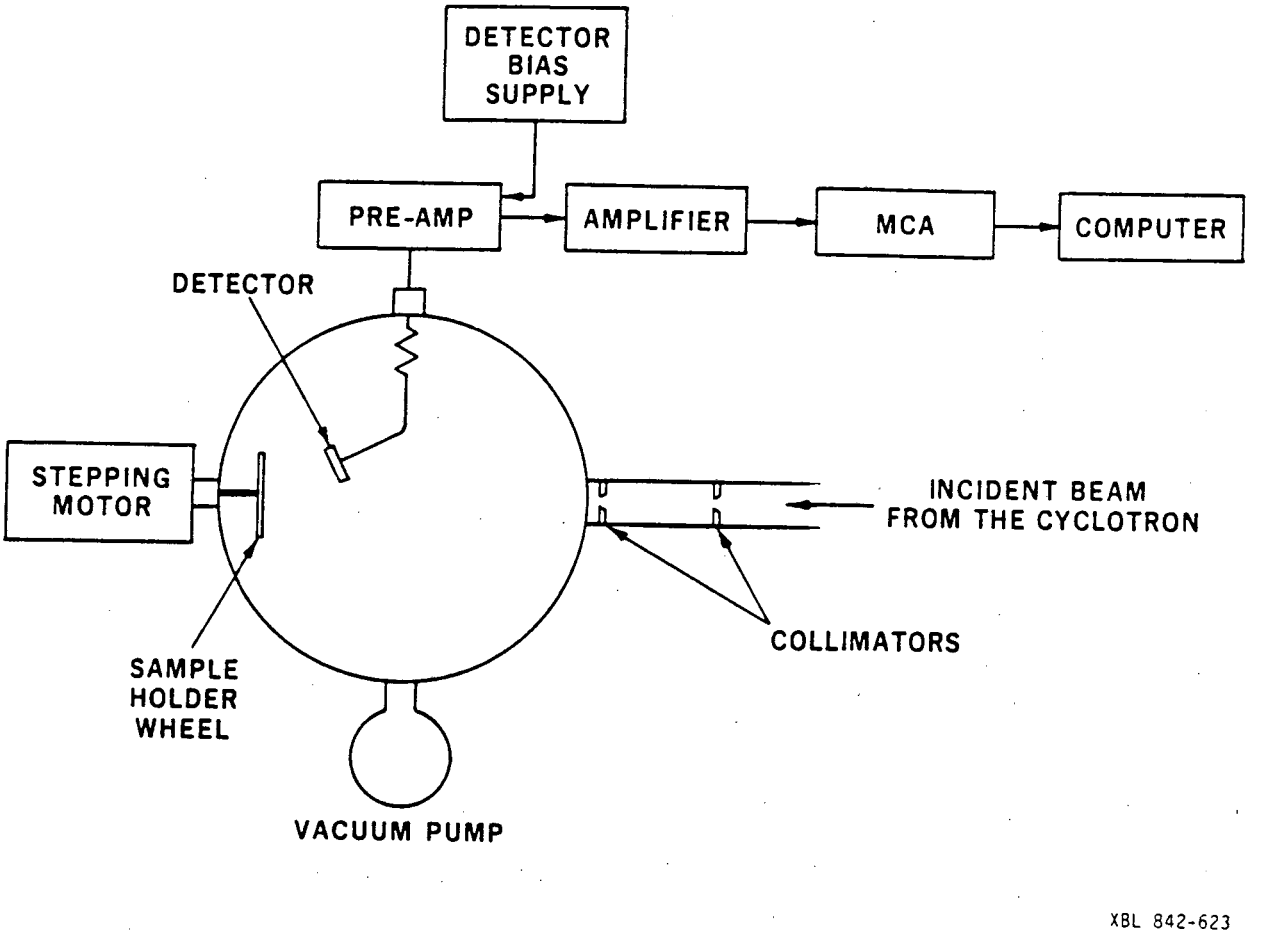

Fig. 4.9 Simplified schematic diagram for HIRBS experimental set up.

4.4.1 Mass Resolution Study

In section 4.2.2, the improved mass resolution of HIRBS was described in detail. In order to verify this, experiments on multi-isotopic elemental samples were carried out. Thin films of Cu and Ag (≈50Å) were deposited on carbon substrates. Cu has isotopes with masses 63 and 65 AMU. According to figure 4.7, these isotopes cannot be resolvable in 1.5MeV $^4He^+$ RBS ($\Delta M_2 \approx 5$AMU at $M_2=60$AMU) but will be nicely separated in HIRBS. Isotopes of Ag with masses 107 and 109 AMU are adequately

resolved in HIRBS but not with α-RBS. Figure 4.10 (a) and (b) show the HIRBS spectra for Cu and Ag films. The completely separated peaks in the case of Cu and the partially separated doublets in the case of Ag verified, without ambiguity, the improved mass resolution of HIRBS. Furthermore, the relative abundances of the isotopes in the elements were also calculated by comparing the total yield under the peaks. For Cu, the relative abundances of ^{63}Cu and ^{65}Cu were 69.4% and 30.6%, while for ^{107}Ag and ^{109}Ag they were 54% and 46%. These match with the tabulated results to within 5% error.

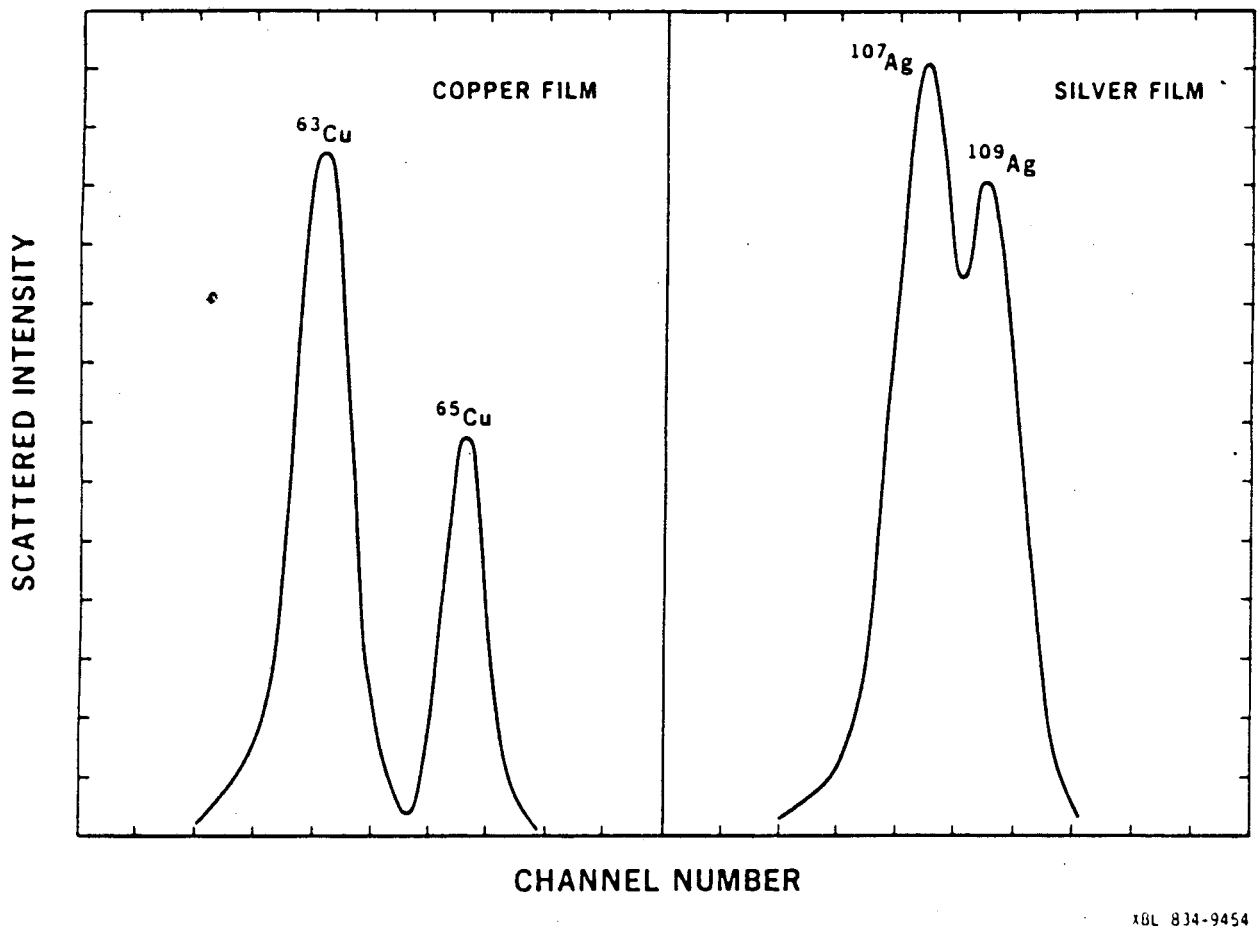

Fig. 4.10 Spectra obtained from 50Å layers of natural Cu and Ag using 20MeV ^{16}O as projectiles.

HIRBS measurements on a piece of bare Ge was also made. The five isotopes in Ge : ^{70}Ge, ^{72}Ge, ^{73}Ge, ^{74}Ge and ^{76}Ge were well resolved in the HIRBS spectrum shown in figure 4.11. The relative abundances of the five isotopes of Ge can be approximated by the relative heights of the five steps in the Ge edge in the spectrum.

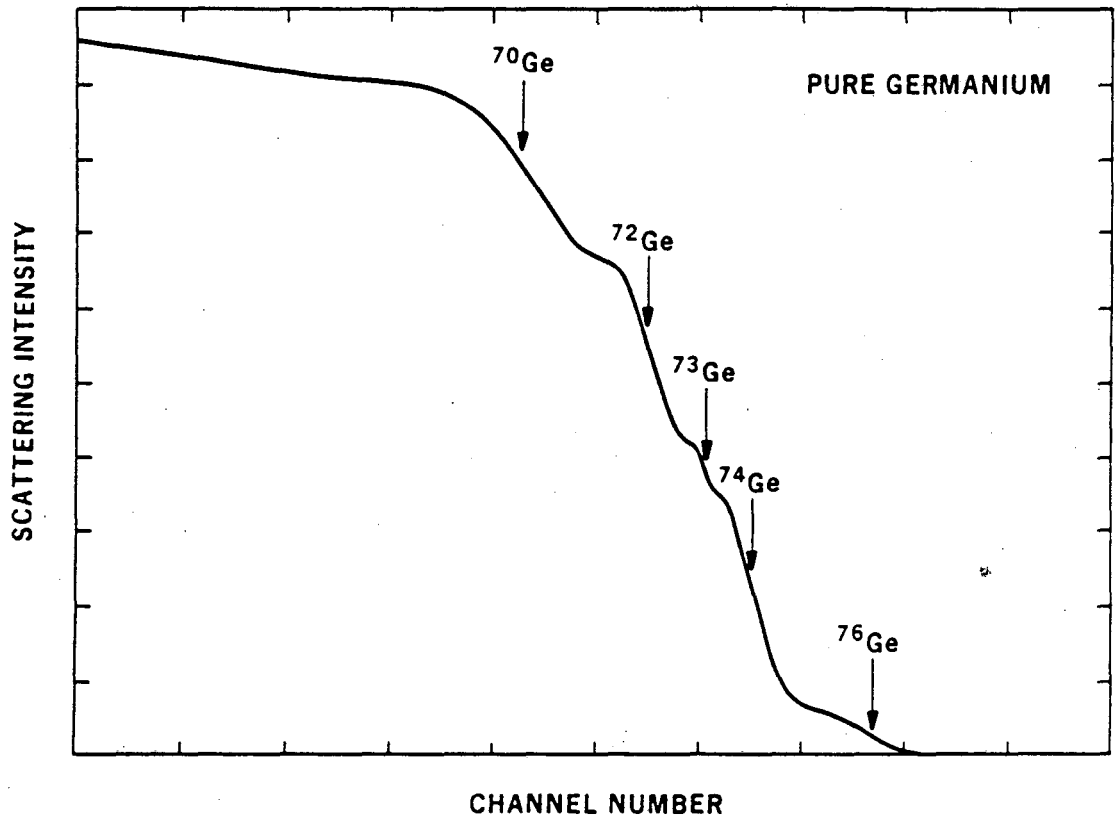

XBL 842-619

Fig. 4.11 Backscattering spectrum for 20MeV ^{16}O ions incident on a bare Ge sample.

4.4.2 Ion Implantation Study

An important consideration in the study of ion implantation profiles when using backscattering method is signal overlap between the substrate edge and the impurity peak in the

backscattering energy spectrum. The profile of the dopant impurity in the substrate can be measured only when the impurity mass is larger than the substrate mass and overlapping of the substrate and impurity signals does not occur. Therefore one can define the maximum identifiable implantation depth of an impurity species below the substrate surface as

$$(R_p)_{max} = \frac{(K_{imp}-K_{sub})E_o}{[S]_{imp}^{sub}} - \frac{1}{2}\Delta R_p \qquad (4.8)$$

where K_{imp} and K_{sub} are the impurity and substrate kinematic scattering factor respectively and $[S]_{imp}^{sub}$ is the energy loss factor when the particles pass through the substrate scattered by an impurity atom. $[R_p]_{max}$ is also known as the maximum accessible depth for impurity detection.

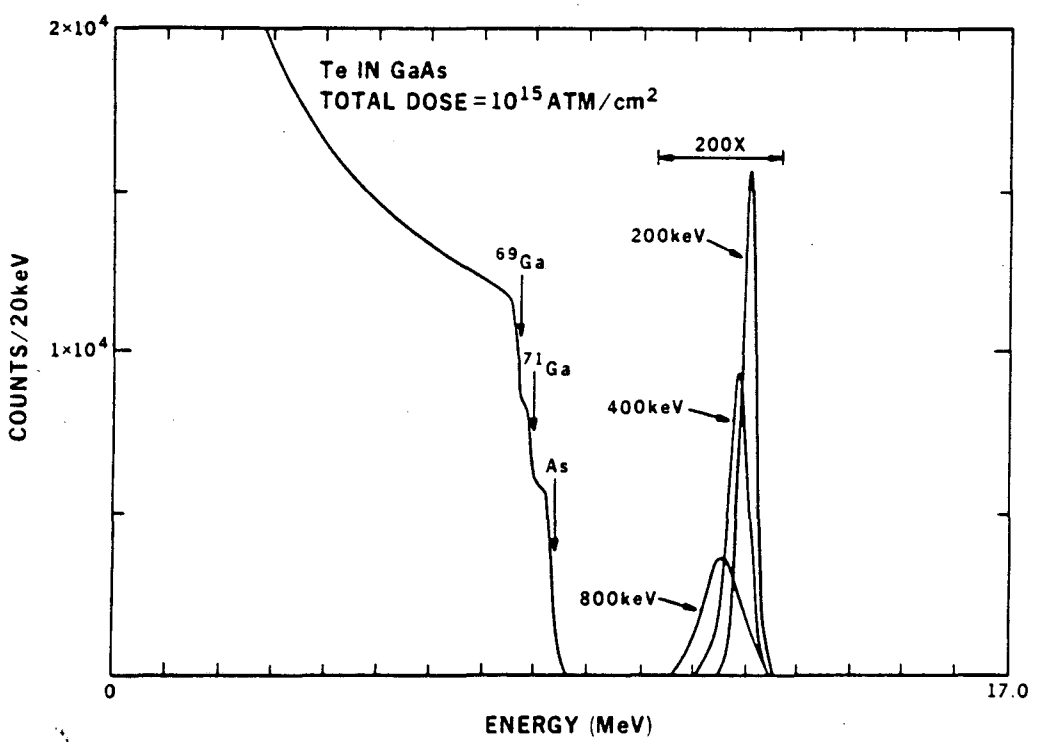

Fig. 4.12 20MeV ^{16}O ion RBS spectra of ^{130}Te implanted GaAs at 200, 400 and 800keV to a dose of 10^{15}atoms/cm^2.

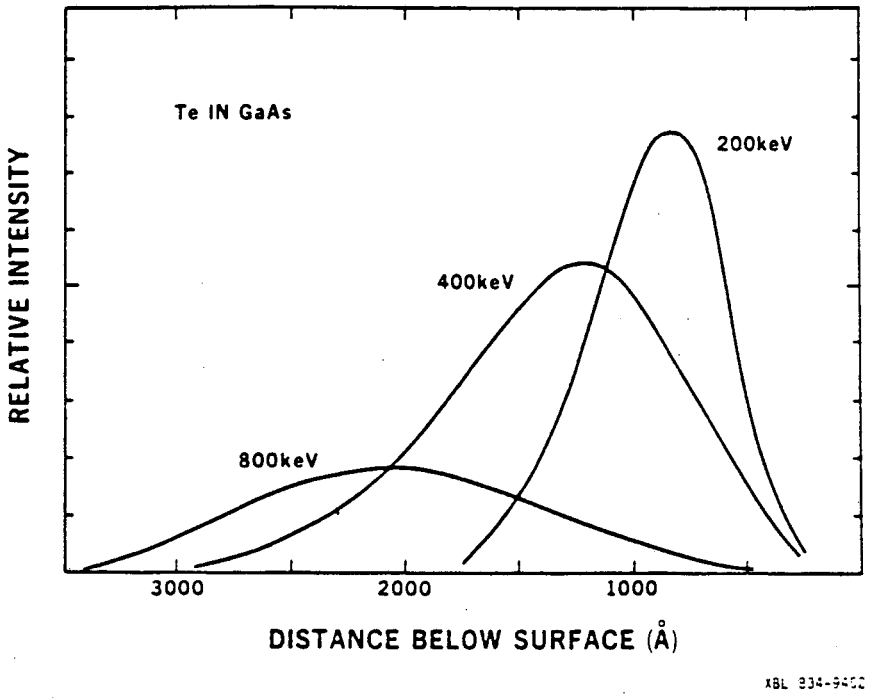

Fig. 4.13 Te concentration profiles in GaAs for 200, 400 and 800keV Te implants as measured by HIRBS.

Studies of ion implantation profiles in compound semiconductors were carried out. Isotopically separated ^{130}Te was implanted at different energies (200keV, 400keV and 800keV) with 10^{15} atoms/cm^2 dose into GaAs substrates. Figure 4.12 shows three HIRBS spectra of ^{130}Te implanted at 200, 400, and 800keV. Note that even for 800keV implantation which corresponds to a R_p of 1900Å and ΔR_p of 900Å, the ^{130}Te peak is still well separated from the GaAs edge. With the known dE/dx values for Te in GaAs, R_p and ΔR_p for each case were measured and the results were within 10% error with the tabulated values calculated with the LSS theory. Figure 4.13 shows the ^{130}Te concentration profile in the GaAs substrates as measured from the spectra. As a comparison, the same systems were analyzed by a 2.0MeV

$^4He^+$ beam. The spectrum for the 400keV implant is shown in figure 4.14. Obviously the Te peak was not as well separated as in figure 4.13. In fact, analysis with the same beam on the 800 keV implant showed that the Te peak was covered entirely by the GaAs signal and no impurity profile was observed.

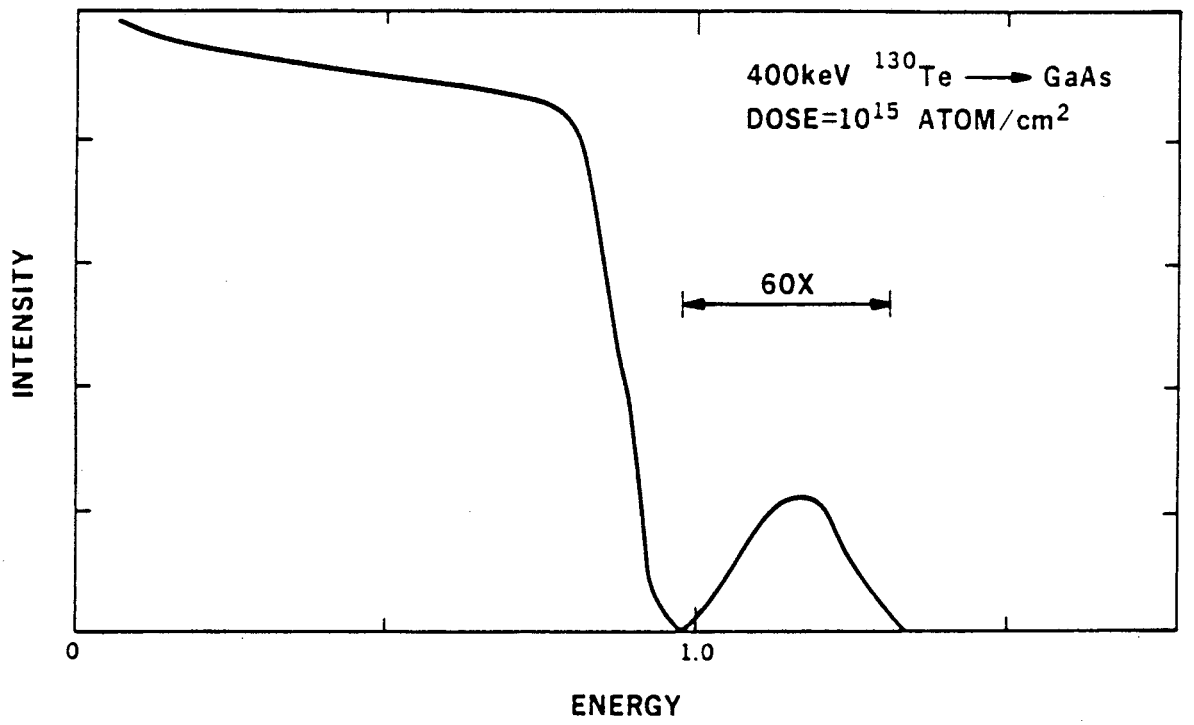

XBL 842-620

Fig. 4.14 2.0 MeV ^{4}He RBS spectrum of 400keV Te implant in GaAs with total dose of 10^{15} atoms/cm^2.

The minimum detectable limit can be defined as the concentration of the impurities corresponding to a net total count equal to three times the standard deviation, i.e., three times the square root of the background counts (95% confidence level of detection)[51]. For RBS analysis, the minimum detection limit of impurities is:

$$(Nt)_{min} = \frac{3\sqrt{A_B}}{\Omega \sigma Q} \tag{4.9}$$

where A_B is the background yield under the impurity signal peak. By this method, the minimum detectable limit for Te in GaAs was estimated from the data obtained to be 4×10^{13} at/cm^2 and this is comparable to the result for ^{4}He RBS. With the application of an annular detector positioned around the beam axis, increase in the geometry efficiency resulted in an improvement in the minimum detectable limit. $(Nt)_{min}$ in this case became 2.5×10^{13} at/cm^2.

Table 4.2 is a summary of the comparison data between ^{16}O and ^{4}He for the use of several impurity substances in two representative substrates, Ge and Si. The depth resolution was calculated using the surface energy approximation for the energy loss factor and assumes an energy resolution of 100keV for ^{16}O and 15keV for ^{4}He. The depth resolution will degrade as a function of depth due to energy loss straggling, especially for heavy ions. From table 4.2, it can be concluded that the depth resolutions are comparable for the two ion beams except for the case of very light or very heavy materials where the two methods exhibit their respective advantages. The accessible depth, however, is significantly greater for heavy ions particularly for the larger mass dopant where the advantage is as great as a factor five. The minimum detectable limit for impurities is comparable for the two methods.

It should also be pointed out that implant species with multiple isotopes were not desirable. The improved mass

resolution of HIRBS would be lost because the various isotopes would produce overlapping peaks. Therefore, isotopically separated implant species must be used in order to have unambiguous impurity distribution determination.

	ACCESSIBLE DEPTH (μm)		DEPTH RESOLUTION (Å)		MINIMUM DETECTION AMOUNT (Atoms/cm^3)	
	^{4}He *	^{16}O **	^{4}He	^{16}O	^{4}He	^{16}O
P ⟶ Si	0.14	0.3	320	570	--	--
As ⟶ Si	1.0	2.5	300	330	--	--
Sb ⟶ Si	1.16	3.4	290	300	6×10^{17}	8×10^{17}
Bi ⟶ Si	1.35	4.1	290	280	—	
As ⟶ Ge	0.01	0.04	260	280	--	--
Sb ⟶ Ge	0.24	0.9	250	250	3×10^{18}	3×10^{18}
Bi ⟶ Ge	0.4	1.5	250	230	--	—

*E_0 = 2.0 MeV, ΔE = 15 keV

**E_0 = 20 MeV, ΔE = 100 keV

Table 4.2 Summary of the comparison data between ^{16}O and ^{4}He beams in RBS analysis.

4.4.3 Germanide Formation Study

In section 3.2.1, the application of α-RBS in the study of metal silicides was discussed in detail. HIRBS can also be used in the study of silicide formations but not much improvement is expected in such analysis. In fact α-RBS is a preferred method over HIRBS in silicide study because depth resolution for HIRBS is worse than that of RBS in the case of light elements such as Si. HIRBS, however, has certain advantages in the investigation of ternary silicides or multiple layered silicides.

Like Si, Ge also forms intermetallic compounds with certain metals at temperature well below the liquid phase. These intermetallic compounds are called metal germanides and they play similar roles in germanium devices as silicides do in silicon devices. A lot of effort has been put on the investigation of silicides but not nearly as much work has been done with germanides [52-55]. This is because of the fact that germanium is used only for special application while Si is the workhorse of the electronic industry.

HIRBS is an ideal tool for the investigation of germanides because germanium has a mass of 72 AMU which is within the range where HIRBS has superior mass resolution over α-RBS. The system analyzed here was a paladium germanide system. Thin film (≈400Å) of Pd was vacuum deposited onto single crystal Ge substrate. Another layer of 500Å Au was then deposited on top. This is a typical structure for a germanium radiation detector. In order to make good contact with low contact resistance and good reliability, intermetallic compounds between Pd and Ge must be formed.

The system was heat treated at 200 and 250°C for 1,2,and 4 hours. These samples were then analyzed by HIRBS and α-RBS. HIRBS results for these measurements are shown in figure 4.15. The samples were all tilted to 60° in order to improve depth resolution. It is obvious from the spectrum that germanide was formed by observing the step in the Ge signal and the lowered and broadened Pd signal. Careful analysis showed that the atomic ratio between Pd and Ge in the middle layer is 2:1 and therefore the compound formed was probably Pd_2Ge. Also from the spectrum, one can see the Au diffusion through the Pd_2Ge layer and accumulated at the interface of Ge and Pd_2Ge. The possible structure of the system after 200°C anneal for one hour is shown in figure 4.16. Annealing at 200°C for different time up to four hours showed the same results.

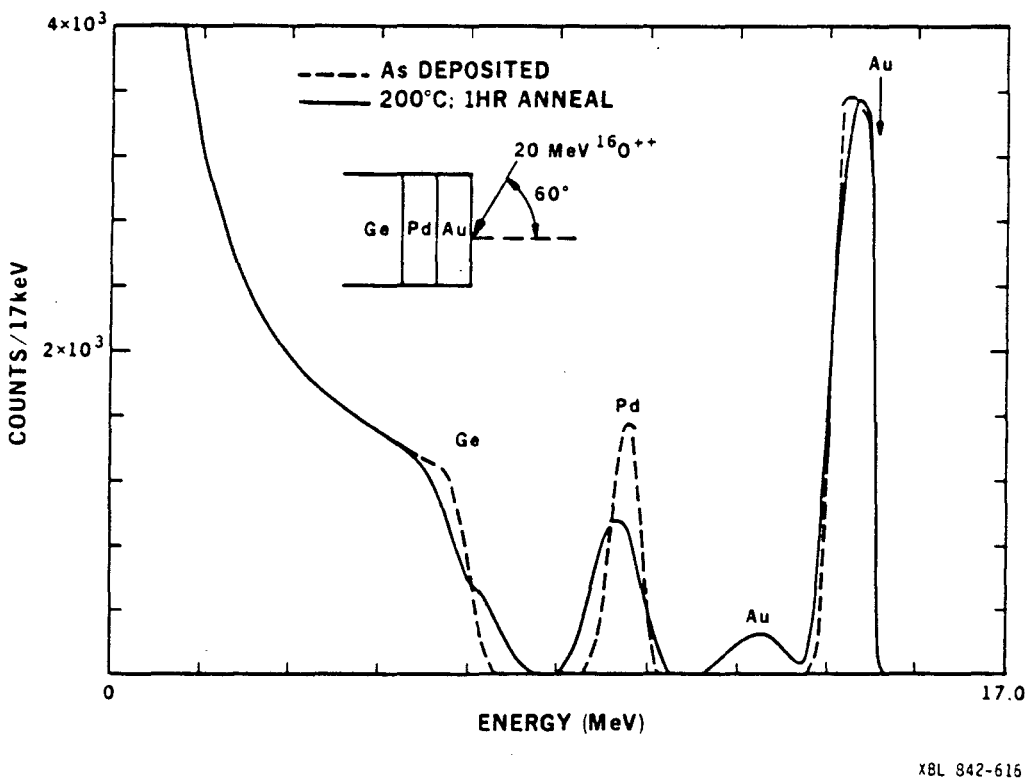

Fig. 4.15 20MeV ^{16}O RBS spectrum for a Au/Pd on Ge system. The solid spectrum represents the 200°C anneal for 1 hour case.

Ge SUBSTRATE	780Å Ge +≈3.4at% Au	700Å Pd_2 Ge +≈1at% Au	500Å Au

XBL 843-946

Fig. 4.16 Possible structure of the Au/Pd on Ge system after 200°C anneal for 1 hour as measured by HIRBS.

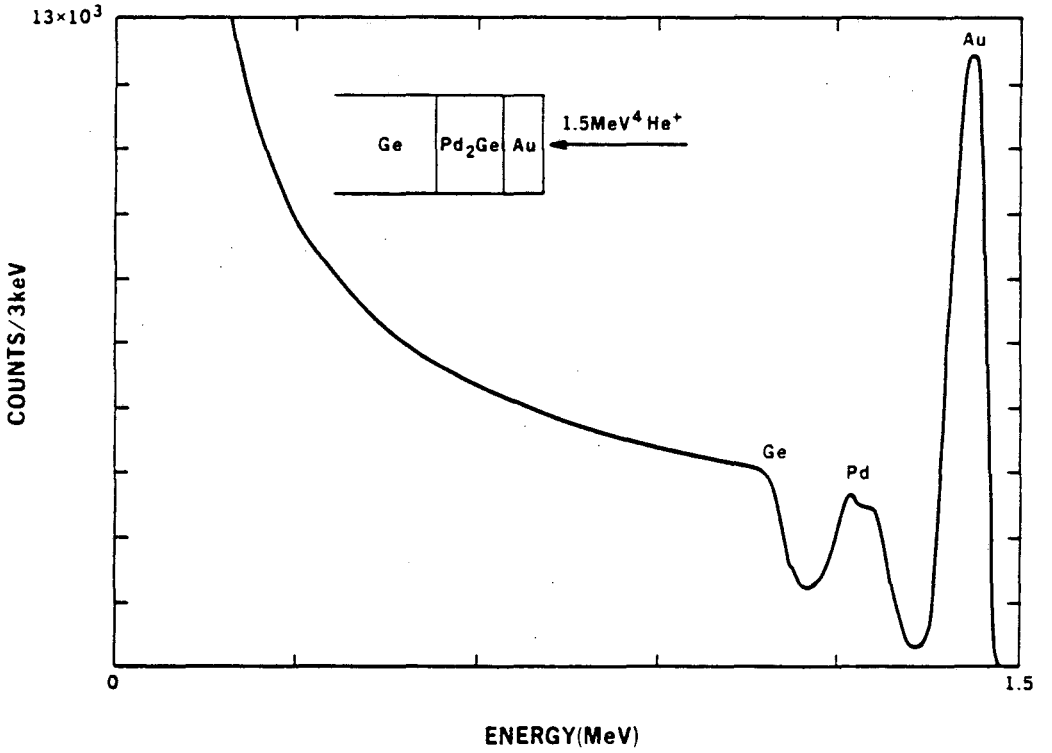

XBL 842-618

Fig. 4.17 1.5MeV ^{4}He RBS spectrum of the Au/Pd on Ge system after annealing.

Analysis of the same system with a 1.5MeV ^{4}He beam, however, gave ambiguous results. Figure 4.17 is an α-RBS spectrum of the system after 200°C anneal for one hour. The Ge and Pd signals overlapped and the Au diffusion was not observable. From the α-RBS spectrum the Pd and Ge atomic ratio in the reacted region cannot be measured. From the above comparison, it is obvious that in this film interaction study, HIRBS is the superior tool.

4.4.4 Multiple Layers Structures on Compound Semiconductors

Another important application of HIRBS involves the study of multiple layered contact structures in III-V compound semiconductor devices, in particular GaAs devices. Typical Schottky and Ohmic contacts for GaAs consist of multiple layers of metals on the GaAs substrates. Detail structural analysis of these systems are usually very difficult with α-RBS. HIRBS, with its advantage of excellent mass resolution in the heavy region, is very suitable for such characterizations.

Figure 4.18 shows a comparison of 20MeV ^{16}O backscattering spectrum with 1.5MeV ^{4}He spectrum for the case of a Schottky contact consisting of a sequence of 500Å Au, Pt and Cr layers on a GaAs substrate. The improved detail of the HIRBS spectrum is obvious. In particular, the Au and Pt layers are easily resolved and their thicknesses unambiguously measured in the HIRBS spectrum whereas they are not resolved by conventional RBS.

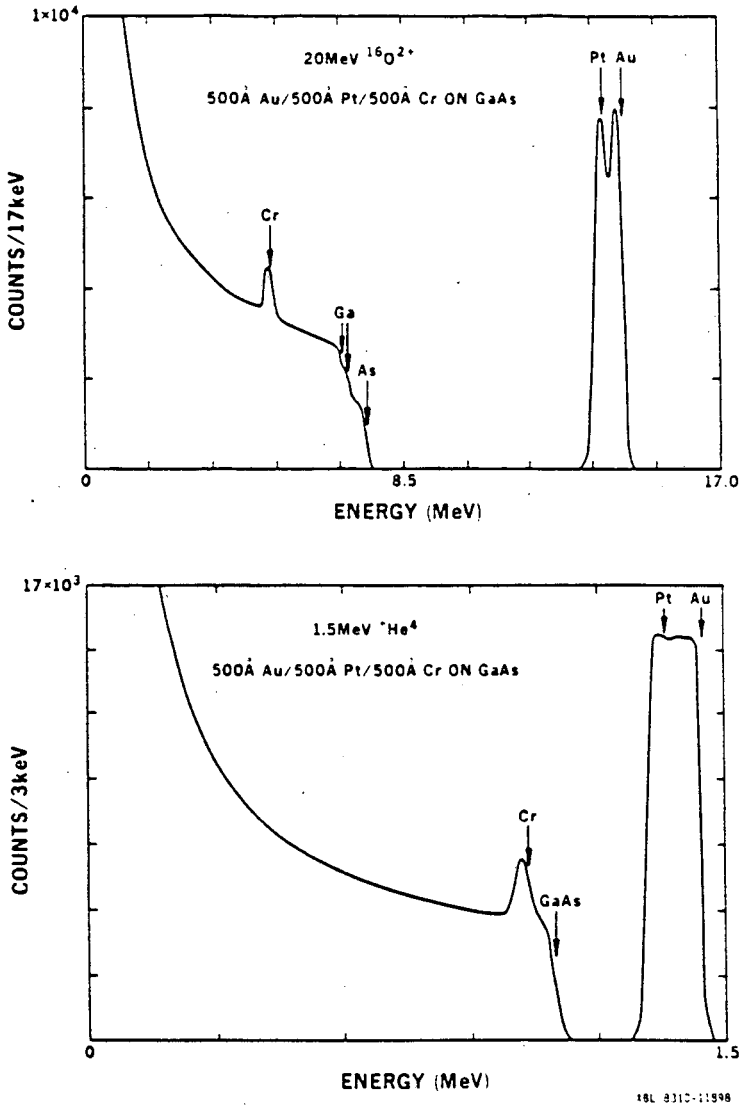

Fig. 4.18 Backscattering spectra comparing ^{16}O and ^{4}He ions RBS for a layered structure consisting of 500Å Au, Pt and Cr on a GaAs substrate.

Figure 4.19 is another comparison of HIRBS and α-RBS analyses. The system analyzed was an Ohmic contact with layers of Au, Ge, Au, Ni/Cr, GaAs on GaAlAs. All layers are well resolved in the HIRBS spectrum and the atomic ratio in the Ni/Cr layer can be measured. In the α-RBS sepectrum, signal overlapping causes a

lot of difficulties in the data analysis. Determination of the layer thicknesses and Ni/Cr ratio is almost impossible.

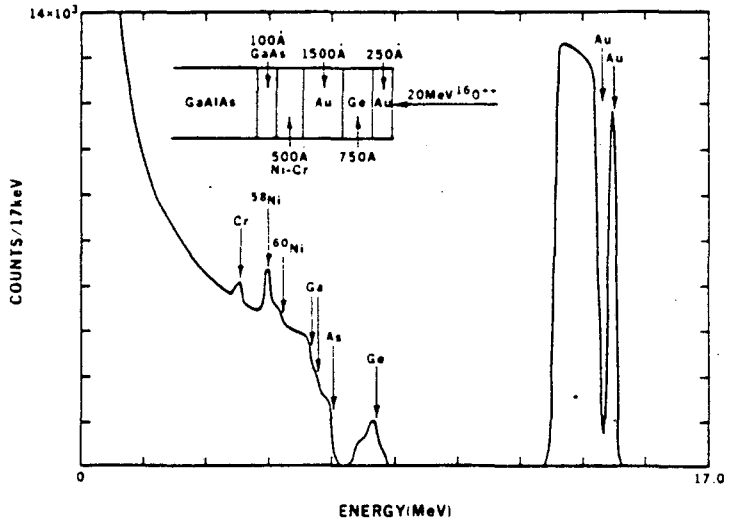

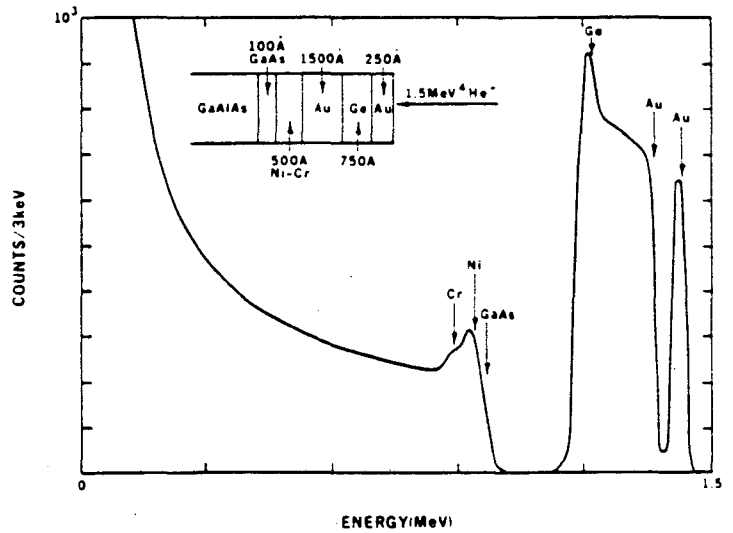

Fig. 4.19 Backscattering spectra comparing ^{16}O and ^{4}He ions RBS for an Ohmic contact structure (250Å Au/750Å Ge/1500Å Au/ 500Å Ni-Cr/100Å GaAs) on GaAlAs substrate.

4.5 Future Development--HIRBS/Channeling

The advantages of channeling with high energy heavy ions arise from the fact that a heavy ion beam trajectory will have greater rigidity with respect to the exchange of transverse momentum. This results in a more pronounced channeling phenomenon with enhanced sensitivity to defects or dopants profile studies.

4.5.1 Dechanneling in a Perfect Crystal

When an ion beam is oriented along a major crystallographic axis, it will exhibit the channeling effect. Dechanneling of these channeled ions arises even in a perfect crystal due to scattering by electrons and the thermally vibrating nuclei in the crystal. This dechanneling effect is observed as the increase in the yield in the backscattering spectrum as a function of the penetration depth of the ions. Theoretical calculations for dechanneling have been carried out by many authors[56-58] based on the continuum approximation[45] in which the motion of the channeled ions is determined by their transverse energy, i.e. their momentum perpendicular to a row of atoms. For particles with a given transverse energy $E_\perp$, the rate of change of $E_\perp$ with penetration depth z averaged over the area $A(E_\perp)$, $\langle dE_\perp/dz \rangle$ is approximately equal to the rate of increase of transverse energy due to multiple scattering. The area $A(E_\perp)$ is the area in the transverse plane accessible to particles with transverse energy $E_\perp$. This rate of increase of transverse energy due to multiple

scattering may be written as the sum of nuclear and electronic contributions. In terms of the reduced transverse energy $\varepsilon_\perp$ ($\varepsilon_\perp = E_\perp / (1/2\ E\ \psi_1^2)$ with $E\ \psi_1^2 = Z_1 Z_2 e^2/d$):

$$\frac{d\varepsilon_\perp}{dz} = \left(\frac{d\varepsilon_\perp}{dz}\right)_n + \left(\frac{d\varepsilon_\perp}{dz}\right)_e \tag{4.10}$$

For particles with low transverse energies, i.e. best channeled particles, the electronic contribution can be much larger than the nuclear contribution. Moreover, both the electronic and nuclear terms in the above equation were shown to be proportional to Z_1/E [42], therefore

$$\left\langle\frac{d\varepsilon_\perp}{dz}\right\rangle \sim \frac{Z_1}{E} \tag{4.11}$$

For a well-collimated beam incident on a structurally perfect crystal surface, the initial normalized distribution of transverse energy $g(\varepsilon_\perp, z)$ will initially be determined mostly by the dominating electronic multiple scattering.

For individual beam particles the changes in transverse energy at successive scatterings are in the nature of a random walk process, there being a net drift toward higher transverse energies. The distribution in transverse energy can therefore be described by a diffusion equation[42, 56]:

$$\frac{\partial g(\varepsilon_\perp, z)}{\partial z} = \frac{\partial}{\partial \varepsilon_\perp}\left[A(\varepsilon_\perp) D(\varepsilon_\perp) \left(\frac{d}{d\varepsilon_\perp} \frac{g(\varepsilon_\perp, z)}{A(\varepsilon_\perp)}\right)\right] \tag{4.12}$$

where $D(\varepsilon_\perp)$ is a diffusion function. Once the initial distribu-

tion $g(\varepsilon_\perp,0)$ is given, then $g(\varepsilon_\perp,z)$ can be found by solving equation 4.12.

With the assumption that particles with transverse energies greater than some value $\varepsilon_\perp^c$ are dechanneled, then the dechanneled fraction as a function of depth is given by:

$$1-f_{ch}(z) = \int_{\varepsilon_\perp^c}^{\infty} g(\varepsilon_\perp,z)d\varepsilon_\perp \qquad (4.13)$$

From the above derivations, it is obvious that explicit functional relations between the dechanneling fraction and Z_1 and E are difficult to obtain. However, by solving equations 4.12 and 4.13 numerically[57.59] the dechanneling fraction was shown to increase as Z_1 increased and decrease as E increased. If we assume that the dechanneling fraction has a simple linear dependence with Z_1 and E ($\approx Z_1/E$), then for a 20 MeV ^{16}O beam, Z_1/E is 0.4. Comparing to a 2MeV ^{4}He beam which has Z_1/E equals 1, there is a factor of 2.5 decrease in dechanneling. This means that HIRBS/channeling has a much more pronounced channeling result.

4.5.2 <u>Dechanneling by Defects</u>

In the presence of lattice defects such as interstitials, dislocation lines, dislocation loops, stacking faults,etc., the backscattered yield is ennanced due to both dechanneling and direct scattering. This is discussed in section 3.2.3. For the case of edge dislocations which have negligible direct scattering, the aligned yield due to the defect is given by equation

3.12. χ_D, the normalized yield due to defect dechanneling is a very sensitive function of λ, the dechanneling cross section given in equation 3.13

$$\lambda L = kE^{1/2} \sim \left(\frac{E}{Z_1}\right)^{1/2} \tag{3.13}$$

When using a 20 MeV ^{16}O beam, λ is enhanced by a factor of 1.6 as compare to using a 2 MeV ^{4}He beam. This dechanneling factor enhancement couples with the reduction in dechanneling of the virgin crystal greatly increase the sensitivity for the detection of line defects in a single crystal.

However, HIRBS/channeling is not very suitable for the detection of point defects such as interstitials which have dechanneling factor $\sigma^D \sim (Z_1/E)$. Using high energy heavy ions, σ_D is reduced. Furthermore, for intersititials, direct scatterings events between projectiles and defects must be considered. The cross section for these events follow the Rutherford scattering cross section which is proportional to $(Z_1/E)^2$. Therefore, it is obvious that HIRBS/channeling is not an ideal tool for point defect analysis since it results in a decrease in the sensitivity of detection of the defects.

Finally, it is important to be aware of the fact that channeling with high energy heavy ions is relatively more difficult to do. The half angle for channeling $\psi_{1/2}$ as given in equation 3.9 is proportonal to $(Z_1/E)^{1/2}$ and is of the order of 1 degree. For HIRBS/ channeling, the $\psi_{1/2}$ is reduced by a factor

of 1.6. Figure 4.20 shows a plot of ψ_1 versus beam energy for ^{4}He and ^{16}O beams in <110> Ge channel. In other words, for HIRBS/channeling, it is more difficult to align the sample so that channeling occurs. Therefore a better collimated beam and a high precision goniometer are required.

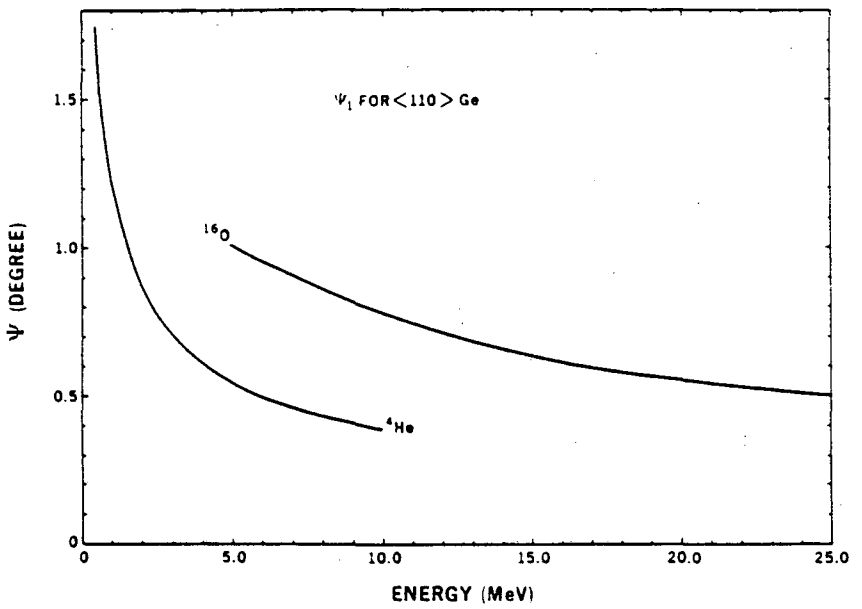

Fig. 4.20 Plots of ψ_1 as a function of beam energy for ^{4}He and ^{16}O beams in <110> Ge channel.

5. SUMMARY

5.1 Advantages

The advantages of HIRBS were well verified in the experimental results described in the previous sections. They can be summarized as follows:

(i) In the case of ion implantation profile studies, HIRBS can increase the accessible depth for analysis. Hence, implantation profiles of higher energy can be studied. This is of particular importance in the study of three dimensional devices in which the implantation energy is in the MeV range.

(ii) In the case of multiple layer metallization structures on heavy semiconductors, the improved mass resolution of HIRBS for heavy elements resulted in unambiguous determination of layer thicknesses and more detail analysis could be carried out.

(iii) In the field of thin film interactions for heavy materials such as germanide formation study, the improved mass resolving power of HIRBS gave better atomic ratio analysis. As a result, the compounds formed in the interactions could be better studied.

(iv) Since the backscattering yield is proportional to $(Z_1Z_2/E)^2$, the use of heavy ion with low energy(<1MeV) is a very good tool for the study of trace amount of heavy surface impurities. The sensitivity could be increased by more than two orders of magnitudes [40].

(v) The fact that no backscattering signal is expected for targets with masses less than the projectiles could be used to increase sensitivity for the detection of trace elements in light substrates.

(vi) In the channeling mode, HIRBS provides information about extended defects profiles with enhenced detection sensitivity due to ennenced defect dechanneling and reduced dechanneling by the virgin crystal.

5.2 Limitations

Apart from the many advantages of HIRBS, this new technique also has certain limitations as a near surface layer analytical characterization technique. Some of these limitations are listed as follows:

(i) Since light targets with masses less than that of the projectiles cannot be detected, impurities such as O, N, C are not detectable in HIRBS when ^{16}O beam is used.

(ii) The good mass resolution for HIRBS also has a disadvantage. It amplifies the isotopic effects for multi-isotopic dopants and layers so that accurate determination of thickness for thin film layers, or ΔR_p for ion implantation profiles are difficult. This shortcoming can easily be remedied by the use of monoisotopic materials.

(iii) The decrease of K value and the worsening of depth resolution of HIRBS for low Z materials make it quite useless

for the characterization of such materials. Figure 5.1 shows a comparison for a silicide system analyzed by 1.75MeV ^{4}He RBS and 20MeV ^{16}O RBS. Obviously the conventional RBS spectrum shows much more detail of the system.

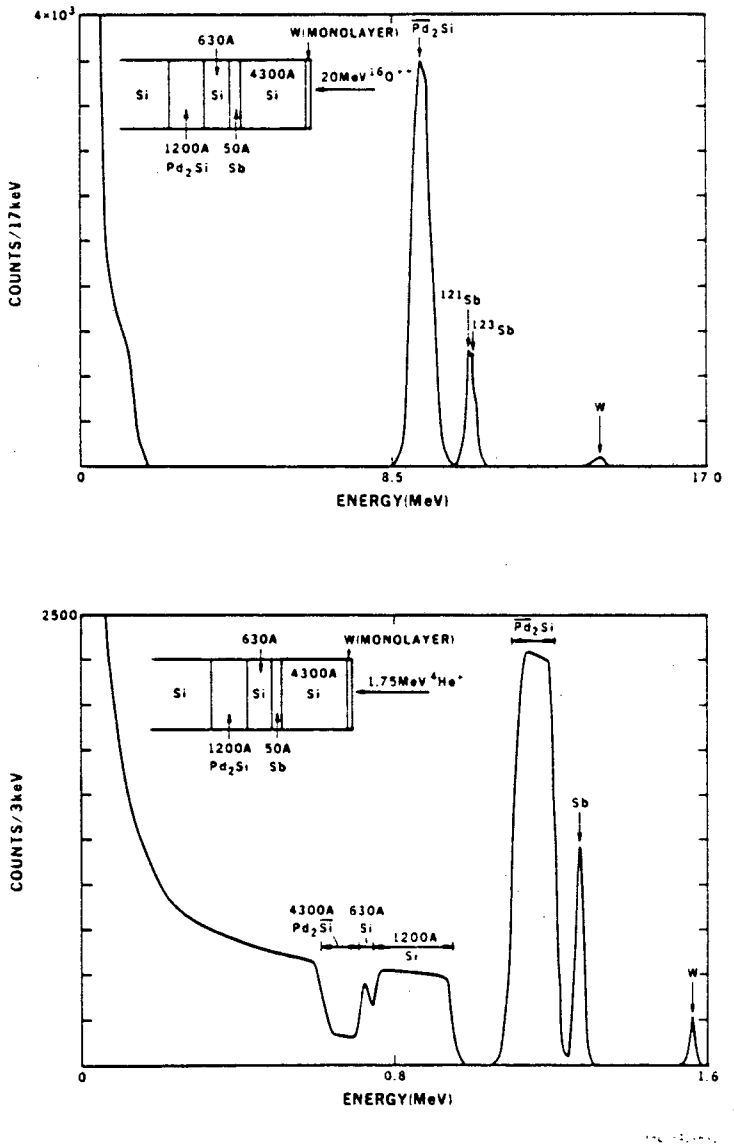

Fig. 5.1 Backscattering spectra comparing ^{16}O and ^{4}He ions RBS for a silicide system.

(iv) Detector lifetime is reduced when heavy ions are used.

(v) Energy loss straggling is important in HIRBS when thick layers (>2000Å) are analyzed. This must be accounted for in order that accurate data analysis can be carried out.

REFERENCES

1. Hart R R, Dunlap H L, Kohr A J, and Marsh O J, Thin Solid Films 19, 137 (1973).

2. Meek R L, J. Electrochem. Soc. 121, 172 (1974).

3. Williams J S, Nucl. Instrum. Meth. 149, 207 (1978).

4. Furukawa S, Matsumura H, and Ishiwara H, Thin Solid Films 19, 399 (1973).

5. Santry D C and Werner R D, Nucl. Instrum. Meth. 139, 135 (1976).

6. Yin S, Zhang J, Gu Q, Lin S, Xie B, Ma T, and Qu Z, Nucl. Instrum. Meth. 191, 147 (1981).

7. Olowolafe J O, Nicolet M-A, Mayer J W, Thin Solid Films 38, 143 (1976).

8. Ottaviani G, J. Vac. Sci. Technol. 16, 1112 (1979).

9. Poate J M, Nucl. Instrum. Meth. 191, 39 (1981).

10. Nava F, Nobili C, Ferla G. Iannuzzi G, Queirolo G, and Celotti G, J. Appl. Phys. 54, 2434 (1983).

11. Wittmer M, J. Appl. Phys. 54, 5081 (1983).

12. Sippel R F, Phys. Rev. 115, 1441 (1959).

13. DeBonte W J, Poate J M, Melliar-Smith C M, and Levesque R A, J. Appl. Phys. 46, 4284 (1975).

14. Poate J M, Turner P A, DeBonte W J, and Yahalom J, J. Appl. Phys. 46, 4275 (1975).

15. Suni I, Nicolet M-A, and Maenpaa M, Thin Solid Films 79, 69 (1981).

16. Picraux S T, Rimini E, Foti G, and Campisano S U, Phys. Rev. B18, 2078 (1978).

17. Swanson M L, Howe L M, Jackman T E, and Moore J A, Nucl. Instrum. Meth. 194, 165 (1982).

18. Miller J W, Gemmell D S, Holland R E, Poizat J C, Wothington J N, and Loess R E, Phys. Rev. B11, 990 (1975).

19. Feldman L C, Nucl. Instrum. Meth. 191, 211 (1981).

20. Meyer O, Gyulai J, and Mayer J W, Surf. Sci. 22, 262 (1970).

21. Feldman L C, Poate J M, Ermanis F, and Schwartz B, Thin Solid Films 19, 18 (1973).

22 Testardi L R, Meck R L, Poate J M, Roger W A, Storm A R, and Wermick J H, Phys. Rev. B11, 4304 (1975).

23. Rutherford E, Phil. Mag. 21, 669 (1911).

24. Geiger H and Marsden E, Phil. Mag. 25, 606 (1913).

25. Rubin S, Passell T O, and Bailey E, Anal. Chem. 29, 737 (1957).

26. Chu W K, Mayer J W, Nicolet M-A, Backscattering Spectrometry (New York: Academic Press) 1978.

27. Ziegler J F, Handbook of Stopping Cross Sections for Energetic Ions in All Elements (New York: Pergeamon Press) 1980.

28. Bethe H A, Ann. Phys. 5, 325 (1930).

29. Block F, Ann. Phys. 16, 285 (1933).

30. Lindhard J and Wintner A., Mat. Fys. Medd. Dan. Vid. Selsk. 34, No.4 (1964).

31. Bragg W H and Kleeman R, Phil. Mag. 10, S318 (1905).

32. Bohr N, Phil. Mag. 30, 581 (1915).

33. Turkevich A L, Knolle K, Emmert R A, Anderson W A, Patterson J H, and Franzgrate E, Rev. of Sci. Instrum. 37, 168 (1966).

34. Turkevich A L, Franzgrate E J, and Patterson J H, Science 158, 635 (1967).

35. Chu W K, Nicolet M-A, Mayer J W, and Evans Jr C A, Anal. Chem. 46, 2136 (1974).

36. Petrov I, Braun M, Fried T, and Satherblom H E, J. Appl. Phys. 54, 1358 (1983).

37. Tu K N, Chu W K, and Mayer J W, Thin solid Films 25, 403 (1975).

38. Campisano S U, Foti G, Grasso F, and Rimini E, Thin Solid Films 25, 431 (1975).

39. Sze S M, Physics of Semiconductor Devices (New York: John Wiley a Son) 1981.

40. Lindhard J, Scharff M, and Schiott H E, Kgl. Danske. Videnskab. Mat. Fys. Medd. 33, 14 (1963).

41. Barrett J H, Phys. Rev. B3, No. 5, 1527 (1971).

42. Gemmell D S, Rev. Mod. Phys. 46, 129 (1974).

43. Mayer J W and Rimini E eds., Ion Beam Handbook for Material Analysis (New York: Academic Press) 1977.

44. Feldman L C, Mayer J W, Picraux S T, Material Analysis by Ion Channeling-Submicron Crystallography (New York: Academic Press)1980.

45. Lindhard J, Kgl. Danske. Videnskab. Selskab. Mat. Fys. Medd. 36, n14 (1965).

46. Picraux S T, Rimini E, Foti G, and Campisano S U, Phys. Rev. B18, 2078 (1978).

47. Semat H, Introduction to Atomic and Nuclear Physics (New York: Holt, Rinehart and Winston, Inc.) 1971.

48. Northcliff L C and Schilling R F, Nucl. Data Table A7, 233 (1970).

49. Petersson S, Tove P A, Meyer O, Sundqvist B, and Johansson A, Thin Solid Films 19, 157 (1973).

50. Walton J T and Haller E E, paper presented at the Materials Research Society 1982 Annual Meeting, Boston, Ma., Nov. 1-2, 1982.

51. Jaklevic J M, Walter R L, X-Ray Fluorescence Analysis of Environmental Samples ed. by Dzubay T G (Michigan: Ann Arbor Science) 1977.

52. Majni G, Ferrari G, Ferrari R, Canali C, Ottaviani G, Solid State Electron. 20, 551 (1977).

53. Ottaviani G, Canali C, Ferrari R, Majni G, Prudenziati M, and Lau S S, Thin Solid Films 47, 187 (1977).

54. Wittmer M, Nicolet M-A, and Mayer J W, Thin Solid Films 42, 51, (1977).

55. Grimaldi M G, Wielunski L, and Nicolet M-A, Thin Solid Films 81, 207 (1981).

56. Bonderup E, Esbensen H, Andersen J U, and Schiott H E, Rad. Eff. 12, 261 (1972).

57. Matsunami N and Howe L M, Rad. Eff. 51, 111 (1980).

58. Howe L M, Moore J A, Matsunami M, and Wright D R, Rad. Eff. 70, 197 (1983).

59. Bjorkqvist K, Cartling B, and Domeij B, Rad. Eff. 12, 267 (1972)

This report was done with support from the Department of Energy. Any conclusions or opinions expressed in this report represent solely those of the author(s) and not necessarily those of The Regents of the University of California, the Lawrence Berkeley Laboratory or the Department of Energy.

Reference to a company or product name does not imply approval or recommendation of the product by the University of California or the U.S. Department of Energy to the exclusion of others that may be suitable.

TECHNICAL INFORMATION DEPARTMENT
LAWRENCE BERKELEY LABORATORY
UNIVERSITY OF CALIFORNIA
BERKELEY, CALIFORNIA 94720